

Stability of a liquid ring on a substrate

Alejandro G. González^{1,†}, Javier A. Diez¹ and Lou Kondic²

¹Instituto de Física Arroyo Seco, Universidad Nacional del Centro, de la Provincia de Buenos Aires, Pinto 399, 7000, Tandil, Argentina

²Department of Mathematical Sciences, New Jersey Institute of Technology, University Heights, Newark, NJ 07102, USA

(Received 16 May 2012; revised 31 October 2012; accepted 4 December 2012;
first published online 8 February 2013)

We study the stability of a viscous incompressible fluid ring on a partially wetting substrate within the framework of long-wave theory. We discuss the conditions under which a static equilibrium of the ring is possible in the presence of contact angle hysteresis. A linear stability analysis (LSA) of this equilibrium solution is carried out by using a slip model to account for the contact line divergence. The LSA provides specific predictions regarding the evolution of unstable modes. In order to describe the evolution of the ring for longer times, a quasi-static approximation is implemented. This approach assumes a quasi-static evolution and takes into account the concomitant variation of the instantaneous growth rates of the modes responsible for either collapse of the ring into a single central drop or breakup into a number of droplets along the ring periphery. We compare the results of the LSA and the quasi-static model approach with those obtained from nonlinear numerical simulations using a complementary disjoining pressure model. We find remarkably good agreement between the predictions of the two models regarding the expected number of drops forming during the breakup process.

Key words: breakup/coalescence, contact lines, thin films

1. Introduction

Stability of thin films, drops and other liquid structures on solid substrates is important in fluid mechanics. The problem is challenging since it involves modelling free surface flows with fluid domains which may topologically split or merge depending on the instability of the contact lines, where liquid, gas and solid meet. The configurations resulting from these instabilities are characterized by multiple spatial scales, ranging from the one typical of the fluid bulk all of the way down to the microscopic one relevant in the vicinity of the contact lines. From the applications point of view, the unstable evolutions and their final fluid configurations are becoming more and more important particularly in the fields of microfluidics and nanofluidics (Stone, Stroock & Ajdari 2004; Squires & Quake 2005; Baroud, Gallaire & Dangla 2010). The fundamental mechanisms involved in the fluid evolution must be considered in order to understand the formation of drop patterns after eventual breakup of the initial fluid configuration.

† Email address for correspondence: aggonzal@exa.unicen.edu.ar

In order to illustrate the complexity of these problems, note first that even the simplest geometry of uniform fluid films lead to interesting and still unresolved questions particularly at the nanometric scale. The instability development in this configuration is due to destabilizing liquid/solid interaction forces which may lead to so-called spinodal breakup, or to homogeneous or heterogeneous nucleation; see Bonn *et al.* (2009) and Craster & Matar (2009) for recent reviews. Another simple fluid geometry, a rivulet/filament, has also been studied in the literature. Starting from the pioneering paper by Davis (1980), where only marginal stability was considered, a number of extensions ensued (Sekimoto, Oguma & Kawasaki 1987; Langbein 1990; Roy & Schwartz 1999; King, Münch & Wagner 2006; Yang & Homsy 2006; González *et al.* 2007; Diez, González & Kondic 2009; Beltrame *et al.* 2011; Diez, González & Kondic 2012).

These theoretical studies consider infinitely long filaments and, thus, ignore end effects which are inevitably present in the straight finite length filaments present in the experiments. One can also study the breakup of finite length structures without dealing with boundary effects by changing the geometry, i.e. by considering a ring instead of a straight filament. When the width of a ring is small compared with its mean radius, the straight filament problem is recovered, since the additional curvature can now be neglected. However, when the width is comparable to the radius, the curvature becomes an essential aspect of the problem, and its implications are studied in the present work. A similar approach to eliminate boundary effects was considered by Worthington (1879) in connection with the contemporary works of Plateau (1849) and Rayleigh (1879), which dealt with the instability of an infinitely long cylinder in air. Worthington (1879) studied the breakup of a mercury ring falling down from a cast, and therefore not supported by a substrate. Recently, similar experiments using a millimetric water torus immersed in silicone oil were performed by Pairam & Fernández-Nieves (2009).

The inclusion of a supporting substrate has been considered by McGraw *et al.* (2010) for the case of micrometric glassy polystyrene toroids placed on silicon wafers in an atmosphere saturated with toluene. Morphological wetting transitions for ring shaped liquids on lyophobic substrates has been studied by Schafle *et al.* (2010). The geometry of a torus has also been observed in connection with evaporation processes of picolitre drops (Conway, Korn & Fisch 1997; Park & Moon 2006) as well as in the context of molten metals on nanometric scale (Kondic *et al.* 2009). For sufficiently narrow rings, the breakup can be analysed within the straight filament theory (Wu *et al.* 2010, 2011). However, the scenario can become more complex for flat and wide rings, where the thin film instability can compete with the azimuthal breakup.

In order to fully understand the mechanisms in play, it is desirable to be able to make some progress via analytical methods. Even when long-wave theory is used to simplify the Navier–Stokes equations, the resulting problem is still very complex. For example, the contact angle hysteresis must inevitably be included in the problem in order for a static axisymmetric solution to exist. This fact is due to the presence of azimuthal curvature, which induces different capillary pressures at the inner and outer radii. Moreover, lack of translational symmetry removes the possibility of a travelling wave solution, that is steady in a moving frame of reference. However, to our knowledge, there is no straightforward method to introduce the required hysteretic effect within the framework of commonly used models based on fluid–solid interaction via disjoining pressure (de Gennes 1985; Bonn *et al.* 2009). Nevertheless, some efforts have been recently done by implementing efficient numerical methods that simply change the local contact angle according to the variation of the thickness there (Koh

et al. 2009). Additional progress can be reached by considering instead a slip-based model combined with contact angle hysteresis. Such an approach was applied to a straight filament placed across an inclined plane, the configuration in which existence of a static base solution also requires contact angle hysteresis (Hocking & Miksis 1993). For this configuration of a straight filament on an incline, we were able to successfully compare the results of a slip model including hysteresis with physical experiments, and explain the main features of the instability development (Diez *et al.* 2012). In the present paper, we follow a similar approach for the ring problem, which leads to an additional set of issues, such as the competition between the closure of the central hole and the breakup into multiple drops. The model we develop in this paper yields a precise set of predictions regarding this and other questions with and without gravitational effects. We note that since we will not be concerned here with the dynamics of a system far from equilibrium, the slip model as implemented here does not require inclusion of a relationship between the contact line velocity and the contact angle itself.

The outline of the paper is as follows. First, we present the formulation of the problem within the long-wave approximation introducing the boundary conditions and the main elements needed to perform the stability analysis of the static solutions using a slip model (§ 2). Then, we study the static (base) solutions by considering the contact angle hysteresis with and without gravity effects. We discuss in detail the conditions that need to be satisfied for the existence of static solutions (§ 3). Then, in § 4 we perform a linear stability analysis (LSA) by employing a pseudo-spectral method based on an appropriately selected basis of Chebyshev functions. We obtain the marginal stability conditions and study the dependence of the dispersion relations on the parameters of the problem. In § 5 we concentrate on the predictions of the LSA regarding ring breakup and expected number of drops that form as a consequence. Then, we extend the LSA of a static ring to study the instabilities expected for a converging ring by using a quasi-static approximation (§ 6). Finally, the results are compared with those obtained by using a disjoining pressure model to account for solid/fluid interaction forces (§ 7).

2. Model

We begin by presenting the model used to describe the time evolution of a liquid ring on a substrate. Figure 1 shows the geometry of the problem and introduces some of the relevant variables, such as radii and contact angles at the inner and outer edges of the ring. The flow description is performed within the framework of the long-wave theory for thin films with free surfaces. This approach assumes that all slopes are small, and since we shall consider below the same length scales in the out-of-plane and in-plane direction the corresponding Reynolds number must be $o(1)$ or smaller. Modelling dynamics in this context requires some regularizing scheme to deal with the so-called ‘contact line singularity’, which manifests itself as an infinite stress at the line where the three phases, liquid, gas and solid, meet. Numerous approaches to overcome this difficulty exist, as reviewed recently by Bonn *et al.* (2009) and Craster & Matar (2009). In this work we mostly concentrate on a slip model (Dussan V 1976; Greenspan 1978) where the no-slip boundary condition at the fluid–solid interface is relaxed. Thus, instead of having vanishing horizontal velocities at the substrate, i.e. $v_x = v_y = 0$ at $z = 0$, we use the Navier boundary condition

$$v_{x,y}|_{z=0} = \frac{\ell}{3} \frac{\partial v_{x,y}}{\partial z} \quad (2.1)$$

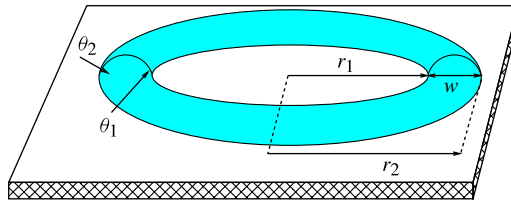


FIGURE 1. (Colour online) Sketch of a fluid ring.

to allow the fluid to slip on the substrate, where ℓ is a prescribed slip length. The above condition is in dimensional variables, but from now on we will use it in dimensionless form by employing the scales as described below. Therefore, the fluid thickness, h , obeys the following dimensionless fourth-order nonlinear partial differential equation (see e.g. Hocking 1990; Hocking & Miksis 1993)

$$\frac{\partial h}{\partial t} + \nabla \cdot [h^2(h + \ell)\nabla\nabla^2 h] - G\nabla \cdot [h^2(h + \ell)\nabla h] = 0, \quad (2.2)$$

where the scale for h , ℓ , and in-plane coordinates is L , while that for time t is $T = 3\mu L/\gamma$. Here, γ is the surface tension and μ the viscosity. The constant G is given by

$$G = L\sqrt{\frac{\rho g}{\gamma}}, \quad (2.3)$$

where g is the gravity and ρ the density. If gravity is not considered, $G = 0$ and the length L can be given by any relevant geometrical property of the problem. On the other hand, when gravity is considered, the natural scale is $L = a$, where $a = \sqrt{\gamma/(\rho g)}$ is the capillary length and, consequently, $G = 1$.

Owing to the symmetry of the problem, it is natural to select polar coordinates (r, φ) for the in-plane variables. At the inner and outer contact lines, we impose the boundary conditions of zero fluid thickness

$$h(R_1(\varphi, t), t) = 0, \quad h(R_2(\varphi, t), t) = 0, \quad (2.4)$$

and prescribed contact angles (see e.g. Davis 1980)

$$\hat{\mathbf{n}} \cdot \nabla h|_{r=R_1} = \tan \theta_1, \quad \hat{\mathbf{n}} \cdot \nabla h|_{r=R_2} = -\tan \theta_2, \quad (2.5)$$

where $\hat{\mathbf{n}}$ is the outward in-plane normal to the contact line, and R_1 , R_2 ($>R_1$) are the radial positions of the contact lines. Initially, $R_1 = r_1$ and $R_2 = r_2$ at $t = 0$ for $0 \leq \varphi < 2\pi$, i.e. both contact lines are circular.

A key feature of this problem is that a static solution requires two different contact angles, that is, θ_1 and θ_2 , at R_1 and R_2 , respectively, as also discussed recently by Chugunov, Schulz & Akhatov (2011). Therefore, we must consider contact angle hysteresis to support a static ring on a homogeneous substrate. The hysteresis of the contact angle may be described by advancing and a receding static angles, θ_{adv} and θ_{rec} , respectively, as also considered by Hocking & Miksis (1993). When one places a ring on a substrate, both contact lines relax until equilibrium is reached for some θ_1 and θ_2 satisfying $\theta_2 \leq \theta_{adv}$ and $\theta_1 \geq \theta_{rec}$.

Consistently with our goal of studying the ring stability, we will consider a basic static solution, $h_0(r, \varphi)$, perturbed by $h_1(r, \varphi, t)$, as

$$h(r, \varphi, t) = h_0(r, \varphi) + \epsilon h_1(r, \varphi, t), \tag{2.6}$$

where $\epsilon \ll 1$. By replacing this expression into (2.2), and retaining only the terms up to order ϵ , we have the equilibrium equation

$$\nabla \cdot [h_0^2(h_0 + \ell) \nabla (\nabla^2 - G) h_0] = 0, \tag{2.7}$$

where the perturbation satisfies

$$\frac{\partial h_1}{\partial t} + \mathcal{L}_1 h_1 = 0, \tag{2.8}$$

and we define

$$\mathcal{L}_1 h_1 = \nabla \cdot [h_0^2(h_0 + \ell) \nabla (\nabla^2 - G) h_1] + \nabla \cdot [h_0 h_1 (3h_0 + 2\ell) \nabla (\nabla^2 - G) h_0]. \tag{2.9}$$

Since we are interested in the stability of an axisymmetric ring, we will restrict the discussion to such rings satisfying $h_0(r, \varphi) = h_0(r)$ in the following section. The LSA of these solutions is then carried out in §4.

3. Static base solution and hysteretic effects

In order to obtain a static solution, we need to solve (2.7). Considering the boundary conditions at the contact lines at fixed radii r_1 and r_2 (see (2.4)),

$$h_0(r_1) = 0, \quad h_0(r_2) = 0, \tag{3.1}$$

and assuming that both $\nabla \nabla^2 h_0$ and ∇h_0 are finite there, we have

$$\nabla [(\nabla^2 - G) h_0] = 0. \tag{3.2}$$

Upon integration we have

$$(\nabla^2 - G) h_0 = p, \tag{3.3}$$

where p is a constant representing the pressure inside the ring. Since $h_0 = h_0(r)$, (3.3) becomes

$$\frac{d^2 h_0}{dr^2} + \frac{1}{r} \frac{dh_0}{dr} - G h_0 + p = 0. \tag{3.4}$$

Integration of (3.4) requires to consider separately the cases with ($G = 1$) and without ($G = 0$) gravity.

3.1. Steady solution without gravity ($G = 0$)

For $G = 0$, we find from (3.4)

$$h_0(r) = -\frac{pr^2}{4} + c_1 \ln r + c_2, \tag{3.5}$$

where c_1 and c_2 are constants. By applying the boundary conditions (3.1),

$$c_1 = p (r_2^2 - r_1^2) / \Delta \tag{3.6}$$

$$c_2 = -p (r_2^2 \ln r_1 - r_1^2 \ln r_2) / \Delta, \tag{3.7}$$

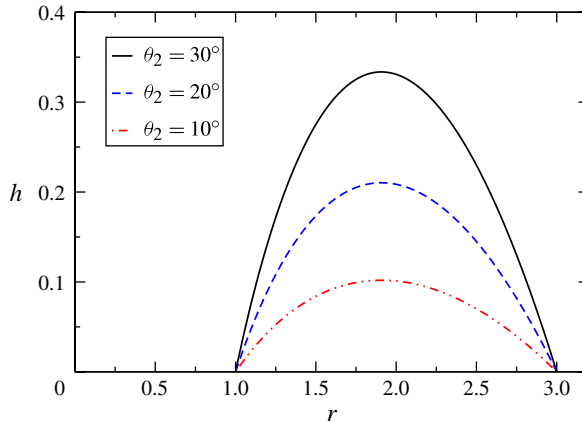


FIGURE 2. (Colour online) Radial thickness profiles for $r_1 = 1$, $r_2 = 3$ and several values of θ_2 without gravity effects ($G = 0$).

where $\Delta = 4 \ln(r_2/r_1)$. To obtain the pressure, p , we must impose the contact angle conditions. By setting $dh_0/dr = -\tan \theta_2$ at $r = r_2$, we have

$$p = -4r_2 \ln(r_2/r_1) \tan \theta_2 / \Delta_1, \quad (3.8)$$

where

$$\Delta_1 = r_2^2 - r_1^2 - 2r_2^2 \ln(r_2/r_1). \quad (3.9)$$

Then, the contact angle, θ_1 , at $r = r_1$ is automatically given by

$$\tan \theta_1 = - \left(\frac{r_2 \Delta_2}{r_1 \Delta_1} \right) \tan \theta_2 \quad (3.10)$$

where

$$\Delta_2 = r_2^2 - r_1^2 - 2r_1^2 \ln(r_2/r_1). \quad (3.11)$$

Note that when one contact angle is given, for instance θ_2 , the other is determined by (3.10). Thus, for given values of r_1 , r_2 and θ_2 the steady solution is completely determined. However, since θ_1 and θ_2 are only limited by the hysteresis range $[\theta_{rcd}, \theta_{adv}]$, we actually have a family of solutions. We note that the volume of the ring is given by

$$V = \pi r_2 \frac{(r_2^2 - r_1^2)^2 - (r_2^4 - r_1^4) \ln(r_2/r_1)}{2\Delta_1} \tan \theta_2. \quad (3.12)$$

Figure 2 shows typical thickness profiles for $r_1 = 1$, $r_2 = 3$ and several values of θ_2 . The asymmetry is more pronounced as θ_2 increases, and the position of maximum thickness moves towards r_1 . Consistently with our previous works (Diez *et al.* 2009, 2012; González *et al.* 2007), we keep factors such as $\tan \theta_2$ without approximating $\tan \theta_2 \approx \theta_2$ although strictly speaking long-wave theory is valid only for small contact angles. Independently of the implementation of the long-wave theory, one expects some influence of the underlying approximation on the results for larger contact angles considered.

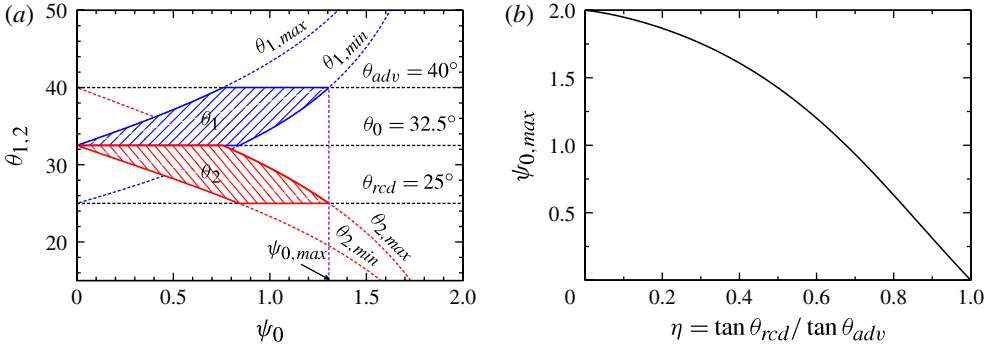


FIGURE 3. (Colour online) (a) Values of θ_1 and θ_2 leading to a static ring for a hysteresis interval $(\theta_{rcd}, \theta_{adv}) = (25^\circ, 40^\circ)$ without gravity effects ($G = 0$). (b) Maximum value of the aspect ratio of the ring, $\psi_{0,max}$, due to hysteresis.

Often, it is more convenient to characterize ring geometry by its mean radius, r_m , and the aspect ratio, ψ_0 , respectively defined as

$$r_m = (r_1 + r_2)/2, \quad 0 < r_m < \infty \tag{3.13a}$$

$$\psi_0 = w/r_m, \quad 0 < \psi_0 < 2 \tag{3.13b}$$

where $w = r_2 - r_1$ is the ring width. The substitution

$$r_1 = r_m(1 - \psi_0/2), \quad r_2 = r_m(1 + \psi_0/2), \tag{3.14}$$

allows us to write (3.10) as

$$\tan \theta_1 = F(\psi_0) \tan \theta_2 \tag{3.15}$$

where

$$F(\psi_0) = \frac{(\psi_0 + 2) [(\psi_0 - 2)^2 \tanh^{-1}(\psi_0/2) - 2\psi_0]}{(\psi_0 - 2) [(\psi_0 + 2)^2 \tanh^{-1}(\psi_0/2) - 2\psi_0]}. \tag{3.16}$$

We note that the dependence on the mean radius, r_m , has disappeared, so that only ψ_0 determines relation between the contact angles.

In the limit of a straight filament ($r_m \rightarrow \infty$ and $\psi_0 \rightarrow 0$ with $w = \psi_0 r_m = \text{const.}$), due to the mirror symmetry with respect to the filament axis, we have equal contact angles at both contact lines, i.e. $\theta_1 = \theta_2 = \theta_0$, where $\theta_0 = (\theta_{rcd} + \theta_{adv})/2$. Hysteresis is not needed to achieve a static filament, consistently with the fact that $F(0) = 1$.

For $\psi_0 \neq 0$ (i.e. for finite r_m), we expect $\theta_2 < \theta_0 < \theta_1$. Thus, both contact angles must be in the intervals $\theta_2 \in [\theta_{rcd}, \theta_0]$ and $\theta_1 \in [\theta_0, \theta_{adv}]$. However, more strict bounds can be established since θ_1 and θ_2 are related by (3.15). In fact, assuming that the inner contact line advances and the outer one recedes, we find that

$$\tan \theta_0 \leq \tan \theta_{1,min} = F(\psi_0) \tan \theta_{rcd} \leq \tan \theta_{1,max} = F(\psi_0) \tan \theta_0 \leq \tan \theta_{adv}, \tag{3.17}$$

while the range of θ_2 is defined by

$$\tan \theta_{rcd} \leq \tan \theta_{2,min} = \tan \theta_0 / F(\psi_0) \leq \tan \theta_{2,max} = \tan \theta_{adv} / F(\psi_0) \leq \tan \theta_0. \tag{3.18}$$

Figure 3(a) shows the allowed values of θ_1 and θ_2 for which a ring is stationary. As an example, we use $\theta_{adv} = 40^\circ$ and $\theta_{rcd} = 25^\circ$, with allowed values of θ_1 and θ_2 inside the hatched areas. Note that allowed values of θ_1 and θ_2 are not necessarily symmetric with respect to θ_0 due to the relationship specified by (3.15).

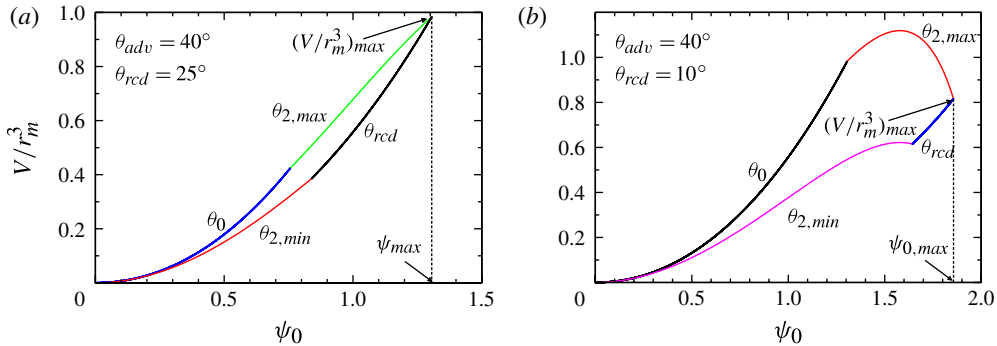


FIGURE 4. (Colour online) Reduced volume, V/r_m^3 , for a static ring without gravity effects ($G = 0$) as the aspect ratio, $\psi_0 = w/r_m$, is varied for two hysteresis ranges. Allowed values are enclosed by the four curve segments, along which θ_2 takes the extreme values permitted by the hysteresis range and (3.17).

In order to determine the maximum possible value of the aspect ratio, $\psi_{0,max}$, one considers the extreme case where $\theta_2 = \theta_{rcd}$ and $\theta_1 = \theta_{adv}$. Then, from (3.15) we have that $\psi_{0,max}$ defined by $\eta F(\psi_{0,max}) = 1$, where $\eta = \tan \theta_{rcd} / \tan \theta_{adv}$ (see figure 3b). We obtain $\psi_{0,max} = 0$ at $\eta = 1$ since this limiting case implies no hysteresis and then no static solution exists. The limit $\eta = 0$ corresponds to $\theta_{rcd} = 0$, so that only wide rings with ($\psi_{0,max} \lesssim 2$) are allowed static solutions.

In terms of ψ_0 and r_m , the ring volume in (3.12) can be written as

$$V = r_m^3 f(\psi_0) \tan \theta_2 = r_m^3 \pi \psi_0 (\psi_0 + 2) \frac{(\psi_0^2 + 4) \tanh^{-1}(\psi_0/2) - 2\psi_0}{2(\psi_0 + 2)^2 \tanh^{-1}(\psi_0/2) - 4\psi_0} \tan \theta_2. \quad (3.19)$$

Therefore, a consequence of the contact angle hysteresis is that for a given volume, V , and mean radius, r_m , there is a range of possible ring widths which lead to a static solution. In fact, by using (3.19) we can transform the hatched region in figure 3(a) for θ_1 or θ_2 into another region for the reduced volume, V/r_m^3 . Figure 4 shows this region, bound by the curves along which θ_2 takes the extreme values permitted by the hysteresis range and (3.17). Note that the same curves would have been obtained if θ_1 were used as a parameter. Thus, for a given volume, V , deposited in the form of a ring with average radius equal to r_m , one can find a range of ψ_0 inside the region where static solutions are possible. Which solution (or ψ_0) is chosen by the system is determined by the initial condition. The two sets of values for θ_{adv} , θ_{rcd} used in figure 4 illustrate the fact that the region where static solutions are possible depends on the hysteresis range, with its size increasing strongly as the hysteresis becomes more pronounced. Note also that as θ_{rcd} approaches θ_{adv} , both the maximum possible reduced volume, $(V/r_m^3)_{max}$, and the aspect ratio, $\psi_{0,max}$, diminish. Interestingly, if θ_{rcd} is very small compared with θ_{adv} , figure 4(b) shows that $(V/r_m^3)_{max}$ is not the absolute maximum of the reduced volume; instead this maximum is achieved at a smaller ψ_0 .

3.2. Steady solution with gravity ($G = 1$)

When gravitational effects are taken into account, the solution $h_0(r)$ of (3.4) for $G = 1$ is given by

$$h_0(r) = c_1 I_0(r) + c_2 K_0(r) + p, \quad (3.20)$$

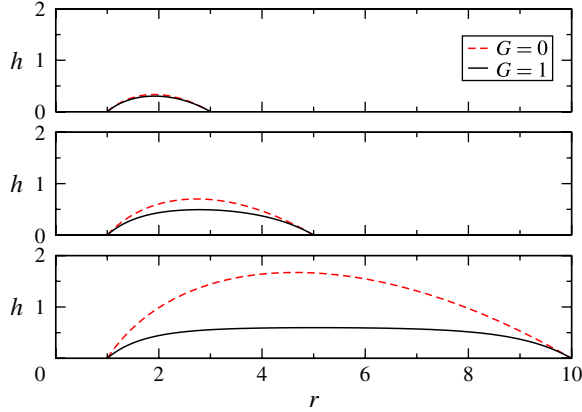


FIGURE 5. (Colour online) Radial thickness profiles for $r_1 = 1$ and $\theta_2 = 30^\circ$ and $r_2 = 3, 5, 10$ with and without gravity.

where I_0 and K_0 are the zeroth-order modified Bessel functions of the first and second kind, respectively. Analogously to the $G = 0$ case, the boundary conditions are that $h_0 = 0$ at $r = r_1$ and $r = r_2$. These conditions lead to

$$c_1 = p [K_0(r_1) - K_0(r_2)] / \Delta, \tag{3.21}$$

$$c_2 = p [I_0(r_2) - I_0(r_1)] / \Delta, \tag{3.22}$$

where

$$\Delta = I_0(r_2)K_0(r_1) - I_0(r_1)K_0(r_2). \tag{3.23}$$

The pressure p is obtained by imposing the contact angle at the outer contact line: $dh_0/dr = -\tan \theta_2$ at $r = r_2$. Thus, we obtain

$$p = \frac{\Delta}{\Delta_1 + \Delta_2} \tan \theta_2, \tag{3.24}$$

where

$$\Delta_1 = I_1(r_2) [K_0(r_1) - K_0(r_2)], \tag{3.25}$$

$$\Delta_2 = K_1(r_2) [I_0(r_1) - I_0(r_2)], \tag{3.26}$$

and I_1 and K_1 are the first-order modified Bessel functions of the first and second kind, respectively. The solution gives the contact angle θ_1 at $r = r_1$ as

$$\tan \theta_1 = - \left(\frac{I_1(r_1)}{I_1(r_2)} \Delta_1 + \frac{K_1(r_1)}{K_1(r_2)} \Delta_2 \right) \frac{\tan \theta_2}{\Delta_1 + \Delta_2} \tag{3.27}$$

and the corresponding ring volume is

$$V = \pi [p (r_2^2 - r_1^2) - 2c_1 (r_1 I_1(r_1) - r_2 I_1(r_2)) + 2c_2 (r_1 K_1(r_1) - r_2 K_1(r_2))]. \tag{3.28}$$

Figure 5 compares the thickness profiles for a ring with $r_1 = 1$ and $\theta_2 = 30^\circ$ and three values of r_2 with and without gravity. We observe that gravity flattens and symmetrizes this profile, so that the volume required for this ring is smaller for given r_1, r_2 and θ_2 when gravity is considered. The effect of gravity is more pronounced as the drop width, w , increases for given r_1 . The profile also becomes more symmetric since the maximum thickness occurs closer to r_m compared with the $G = 0$ case.

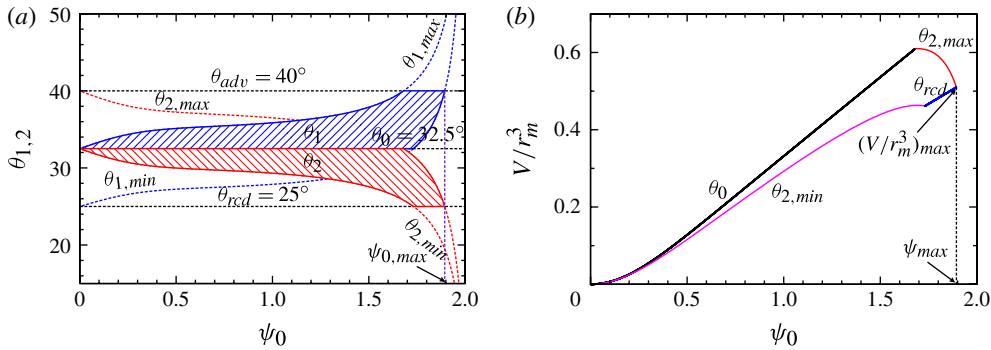


FIGURE 6. (Colour online) (a) Values of θ_1 and θ_2 leading to a static ring solution for a hysteresis interval $(\theta_{rcd}, \theta_{adv}) = (25^\circ, 40^\circ)$ with gravity effects ($G = 1$) and $r_m = 10$; see figure 3(a) for the $G = 0$ case (the results for $G = 0$ are independent of r_m). (b) Reduced volume as a function of the aspect ratio for $G = 1$ with the same parameters as in figure 4(a).

The additional influence of gravity shows when the substitution specified by (3.14) is applied to (3.27). In contrast to the $G = 0$ case, we obtain not only a function of ψ_0 , but also of r_m . Similarly, the reduced volume, V/r_m^3 , depends now on both variables, instead only on ψ_0 . This additional dependence introduces some qualitative and quantitative differences compared with the $G = 0$ case. As expected, these differences are minor for r_m small, $r_m \lesssim 1$ say, but they become considerable for larger r_m . As an example, figure 6(a) shows the diagram of possible contact angles for the same hysteresis range and $r_m = 10$ as in figure 3(a) for $G = 0$. The regions now extend up to a much larger ψ_0 ($\psi_{0,max} = 1.894$), so that wider static rings are possible due to the flattening effect of gravity.

Figure 6(b) shows that the range of the ring volumes leading to static solutions also strongly differs from the corresponding $G = 0$ case (cf. figure 4a). We observe that the effect of gravity is to increase the size of this region, similarly to the effect of larger hysteresis for the $G = 0$ case.

4. Linear stability analysis: techniques and parametric dependence

We carry out the LSA of the static solutions by assuming that one contact angle is given, namely θ_2 , and then θ_1 is determined by (3.10) for $G = 0$ or (3.27) for $G = 1$. We proceed by considering normal mode perturbations of the thickness as

$$h_1(r, \varphi, t) = \hat{h}_1(r) \cos(n\varphi) e^{\omega(n)t} \tag{4.1}$$

and, consequently, perturbations of the positions of the boundaries as

$$R_1(\varphi, t) = r_1 + \epsilon \xi_1 \cos(n\varphi) e^{\omega(n)t}, \tag{4.2}$$

$$R_2(\varphi, t) = r_2 + \epsilon \xi_2 \cos(n\varphi) e^{\omega(n)t}. \tag{4.3}$$

Alternative approaches towards introducing perturbations are possible, one could perturb the contact angle instead of the contact line position for example, as it has been considered in the literature, see the works by Davis (1980) and Langbein (1990) and the recent overview by Diez *et al.* (2009). Here we concentrate only on the perturbation type specified above. We note that the perturbations of the contact lines

are performed for fixed angles θ_1 and θ_2 , so that the perturbed profiles have also contact angles within the hysteresis range.

Only integer values of n (to be called the ‘angular wavenumber’ in the rest of this work) are physically meaningful. Since the perturbations are of the cosine type, without loss of generality, we restrict to $n \geq 0$. After substituting the amplitudes $h_1(r)$, ξ_1 and ξ_2 into (2.2), to the first order in ϵ we obtain the following eigenvalue problem

$$\mathcal{L}_1 \hat{h}_1 = -\omega \hat{h}_1, \tag{4.4}$$

where

$$\mathcal{L}_1 \hat{h}_1 = c_4(r) \hat{h}_{1,rrrr} + c_3(r) \hat{h}_{1,rrr} + c_2(r) \hat{h}_{1,rr} + c_1(r) \hat{h}_{1,r} + c_0(r) \hat{h}_1, \tag{4.5}$$

and the coefficients $c_i(r)$ ($i = 0, \dots, 4$) are given by

$$c_4(r) = H, \tag{4.6a}$$

$$c_3(r) = 2H/r + H_r, \tag{4.6b}$$

$$c_2(r) = -A_2^+ H + H_r/r \tag{4.6c}$$

$$c_1(r) = A_2^- H/r - A_1 H_r, \tag{4.6d}$$

$$c_0(r) = 2(n/r)^2 H_r/r + A_3 H, \tag{4.6e}$$

where

$$H = h_0^2 (h_0 + \ell), \tag{4.7a}$$

$$A_1 = 1/r^2 + (n/r)^2 + G, \tag{4.7b}$$

$$A_2^+ = 1/r^2 + 2(n/r)^2 + G, \tag{4.7c}$$

$$A_2^- = 1/r^2 + 2(n/r)^2 - G, \tag{4.7d}$$

$$A_3 = (-4/r^2 + (n/r)^2 + G) (n/r)^2. \tag{4.7e}$$

Note that $r = r_1$ and $r = r_2$ are singular points of \mathcal{L} , since $H = H_r = 0$ and all coefficients vanish there. As discussed below, our numerical scheme used to solve the eigenvalue problem has a property that the operator is not computed at these points.

The linearized form of the boundary conditions (2.4) and (2.5) yields

$$\hat{h}_1(r_1) + \xi_1 h_{0,r}(r_1) = 0, \quad \xi_1 h_{0,rr}(r_1) + \hat{h}_{1,r}(r_1) = 0, \tag{4.8}$$

$$\hat{h}_1(r_2) + \xi_2 h_{0,r}(r_2) = 0, \quad -\xi_2 h_{0,rr}(r_2) - \hat{h}_{1,r}(r_2) = 0. \tag{4.9}$$

From the known values of the derivatives of h_0 at $r = r_1, r = r_2$, the unknown amplitudes, ξ_1 and ξ_2 , can be eliminated from these four equations, which are then replaced by

$$\hat{h}_{1,r}(r_1) = \frac{h_{0,rr}(r_1)}{h_{0,r}(r_1)} \hat{h}_1(r_1) = \kappa^- \hat{h}_1(r_1), \tag{4.10}$$

$$\hat{h}_{1,r}(r_2) = \frac{h_{0,rr}(r_2)}{h_{0,r}(r_2)} \hat{h}_1(r_2) = \kappa^+ \hat{h}_1(r_2) \tag{4.11}$$

where the constants κ^+ and κ^- are now given by

$$\kappa^- = -\frac{p}{\tan \theta_1} - \frac{1}{r_1}, \quad \kappa^+ = \frac{p}{\tan \theta_2} - \frac{1}{r_2}. \tag{4.12}$$

It is worth noting that κ^- and κ^+ do not depend on either θ_1 or θ_2 . This important fact becomes obvious when the pressure, p , is replaced by the corresponding expressions given in (3.8) and (3.10) for $G = 0$, or (3.24) and (3.27) for $G = 1$.

This completes the formulation of the eigenvalue problem whose solution gives eigenvalues and eigenfunctions. Once this problem is solved, the values of the eigenfunctions at the contact lines allow us to determine their displacements as

$$\xi_1 = -\frac{\hat{h}_1(r_1)}{h'_0(r_1)} = -\frac{\hat{h}_1(r_1)}{\tan \theta_1}, \quad \xi_2 = -\frac{\hat{h}_1(r_2)}{h'_0(r_2)} = \frac{\hat{h}_1(r_2)}{\tan \theta_2}. \tag{4.13}$$

Although the equation for $\hat{h}_1(r)$ is linear, it is fourth order and has variable coefficients, and therefore its solution is not straightforward. Thus, the linear eigenvalue problem must be solved numerically for a given value of n . This is done by discretizing the eigenvalue problem (4.5) using a Chebyshev pseudo-spectral approximation of the derivatives, subject to the boundary conditions given by (4.10) and (4.11).

In order to use Chebyshev functions $T_i(x) = \cos(i \arccos x)$, we express the domain $r_1 \leq r \leq r_2$ as

$$r(\zeta) = r_m \left(1 + \frac{\psi_0}{2} \zeta \right), \tag{4.14}$$

where $-1 \leq \zeta \leq 1$. The boundary conditions given by (4.10) and (4.11) are now more compactly written as

$$g'(\pm 1) = \hat{\kappa}^\pm g(\pm 1), \tag{4.15}$$

where $g(\zeta) = \hat{h}_1(r)$ and $\hat{\kappa}^\pm = \kappa^\pm w/2$. Thus, we rewrite (4.5) in terms of x as

$$\mathcal{L}g = \hat{c}_4(\zeta)g'''' + \hat{c}_3(\zeta)g'''' + \hat{c}_2(\zeta)g'' + \hat{c}_1(\zeta)g' + \hat{c}_0(\zeta)g, \tag{4.16}$$

where $\hat{c}_i(\zeta) = (2/w)^i c_i(r)$. We now look for a solution of the form

$$g(\zeta) = \sum_{i=1}^N \beta_i \phi_{i-1}(\zeta), \tag{4.17}$$

where $\phi_i(\zeta)$ is an orthogonal basis and β_i are unknown spectral coefficients.

A most obvious idea is to take $\phi_i(\zeta) = T_i(\zeta)$. However, this choice is not convenient since the boundary conditions given by (4.15) are not satisfied by this basis, and an iteration procedure is required for their fulfilment, see Hocking & Miksis (1993). Moreover, this choice requires evaluating $g(\zeta)$ and its derivatives at the contact lines ($\zeta = \pm 1$), which are singular points and divergence of high derivatives of $g(\zeta)$ is expected due to vanishing of the corresponding coefficients, see (4.6). Instead, we ask whether there is a linear combination of $T_i(\zeta)$ leading to a basis set $\phi_i(\zeta)$, such that each base function individually satisfies the boundary conditions. The advantage of this approach is that the points $\zeta = \pm 1$ can be safely excluded from the calculation since fulfilment of boundary conditions is guaranteed.

We consider a basis formed as a combination of Chebyshev functions as follows

$$\phi_i(\zeta) = T_i(\zeta) + a_i T_{i+1}(\zeta) + b_i T_{i+2}(\zeta). \tag{4.18}$$

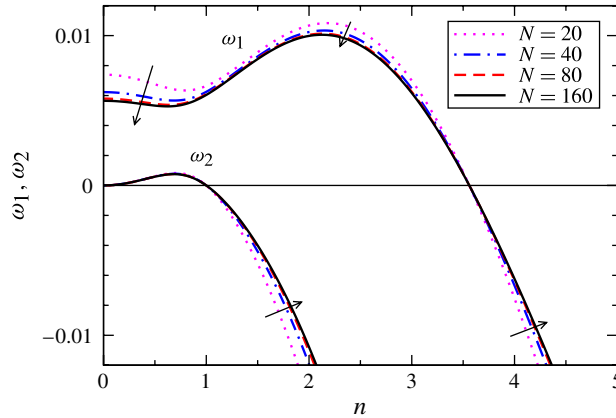


FIGURE 7. (Colour online) Dispersion relations with gravity effects ($G = 1$) $\omega_1(n) > \omega_2(n)$ for $r_1 = 1$, $r_2 = 2$, $\theta_2 = 30^\circ$ and $\ell = 10^{-3}$. The arrows indicate increasing values of N . Note that only integer values of n have physical meaning.

By inserting $\phi_i(\zeta)$ into (4.15), we have two linear equations for the unknowns a_i and b_i ,

$$[(i + 1)^2 + \hat{k}^-] a_i - [(i + 2)^2 + \hat{k}^-] b_i = \hat{k}^- + i^2 \tag{4.19a}$$

$$[(i + 1)^2 - \hat{k}^+] a_i + [(i + 2)^2 - \hat{k}^+] b_i = \hat{k}^+ - i^2 \tag{4.19b}$$

which are easily solved in terms of i , \hat{k}^+ and \hat{k}^- .

By using the Gauss–Lobatto grid (see Boyd 2000),

$$\zeta_i = \cos\left(\frac{\pi i}{N - 1}\right), \quad i = 1, 2, \dots, (N - 2), \tag{4.20}$$

we generate a matrix of dimension $N - 2$ (excluding the grid points $\zeta = \pm 1$) and demand that the residual of the differential equation becomes negligible at the interpolation points on the interior of the interval $(-1, 1)$. Thus, we pose the eigenvalue problem

$$U_{i,j} \beta_i = -\omega V_{i,j} \beta_i, \quad i, j = 1, 2, \dots, (N - 2) \tag{4.21}$$

where

$$U_{i,j} = \hat{c}_4(\zeta_i) \phi_{j-1}''''(\zeta_i) + \hat{c}_3(\zeta_i) \phi_{j-1}''''(\zeta_i) + \hat{c}_2(\zeta_i) \phi_{j-1}''(\zeta_i) + \hat{c}_1(\zeta_i) \phi_{j-1}'(\zeta_i) + \hat{c}_0(\zeta_i) \phi_{j-1}(\zeta_i), \tag{4.22}$$

$$V_{i,j} = \phi_{j-1}(\zeta_n). \tag{4.23}$$

For given n , we choose the two largest eigenvalues, ω_1 and ω_2 , and the corresponding coefficients, $\beta_i^{(1)}$ and $\beta_i^{(2)}$, that give the eigenfunctions by means of (4.17). As we discuss in more detail below, the modes with ω_1 and ω_2 for the ring asymptotically tend to the varicose and (stable) zigzag modes of the filament (Thiele & Knobloch 2003; Diez *et al.* 2009, 2012), respectively.

Figure 7 shows the two largest eigenvalues ω_1 and ω_2 ($\omega_1 > \omega_2$) as a function of n for different numbers of grid points, N . First, we note that due to the lack of translational invariance, the growth rate of the mode $n = 0$ is not zero. We note in passing that

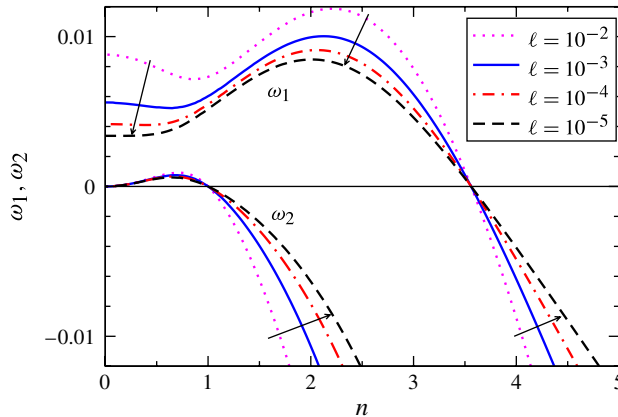


FIGURE 8. (Colour online) Dispersion relations with gravity effects ($G = 1$) for $r_1 = 1$, $r_2 = 2$ and $\theta_2 = 30^\circ$ with decreasing values of ℓ as shown by the arrows. The curves were obtained using $N = 640$.

this mode does not correspond to ring breakup, but instead to a radial collapse of the whole ring into a central drop. Second, there are two other relevant points of these curves, namely, its maximum at (n_{max}, ω_{max}) and its zero at $(n_c, 0)$, which will be analysed below. Next, we see that for the slip length, $\ell = 10^{-3}$, $N = 160$ assures converged results, and therefore we use this value of N whenever such ℓ is considered. When a smaller value of ℓ is chosen, a larger N is required to ensure convergence, as discussed below.

4.1. Effects of the slip length

Figure 8 shows the effect of the slip length on the dispersion relations. Here we use a large value of $N (= 640)$ for which all of the results are fully converged. We see that the main influence of ℓ is to reduce the growth rates of unstable modes and increase the absolute value of stable ones. Note that the marginal angular wavenumbers at which ω_1 and ω_2 vanish do not depend on the slip length, ℓ , indicating that the marginal stability does not depend on the model used to overcome the contact line divergence; this issue is also discussed below in § 5.1. We note that this behaviour is expected as (2.2) represents a gradient dynamics implying that stability thresholds do not depend on the mobility function but only on the second variation of the underlying energy (Mitlin 1993; Thiele 2010).

4.2. Effect of the azimuthal curvature

In order to study how the ring curvature affects its stability, we consider now the dispersion relation for fixed ring width, w , and vary the internal radius, r_1 . As an example, figure 9 shows the dispersion relations, $\omega_1(n)$ and $\omega_2(n)$, for $w = 1$. We will analyse here in detail the limit $r_1 \rightarrow \infty$. We observe that the curve for the ring asymptotically approaches that obtained for the straight filament (dotted line), see Diez *et al.* (2012). In that work, ω_1 was given as a function of the wavenumber q ; for comparison purposes in the present context we can take $n = qr_1$, remembering that only integer values of n have physical meaning. However, to fully understand the limit leading to a straight filament, it is convenient to first discuss the corresponding eigenfunctions.

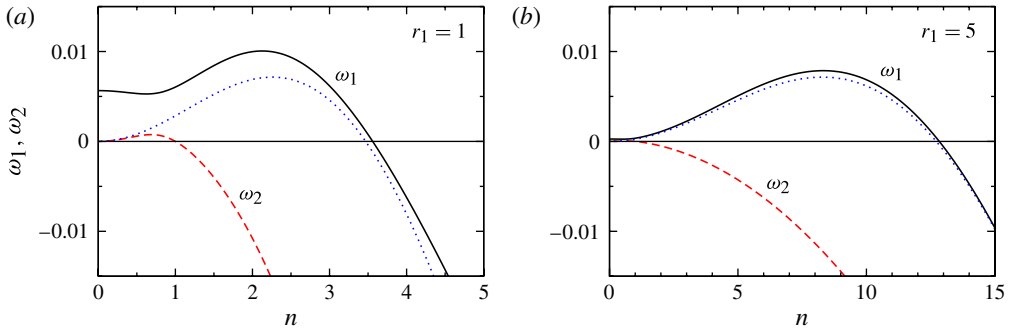


FIGURE 9. (Colour online) Dispersion relations $\omega_1(n) > \omega_2(n)$ for (a) $r_1 = 1$ and (b) $r_1 = 5$. The (blue) dotted line corresponds to $r_1 = \infty$, i.e. a straight filament. Here, $w = 1$, $G = 1$, $\theta_2 = 30^\circ$, $\ell = 10^{-3}$ and $N = 160$.

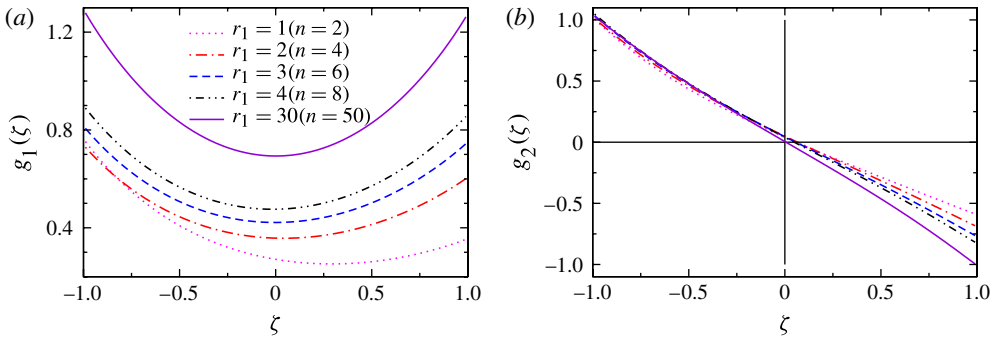


FIGURE 10. (Colour online) Eigenfunctions $g_1(\zeta)$ and $g_2(\zeta)$ for n equal to the integer closest to n_{max} for a few values of r_1 . The rest of the parameters is as in figure 9.

The behaviour of the eigenfunctions, $g_1(\zeta)$ and $g_2(\zeta)$, as r_1 is varied provides additional insight on this limit. First, we consider the eigenfunctions for n equal to the integer closest to n_{max} . Figure 10(a) shows that $g_1(\zeta)$ is strongly asymmetric for small r_1 , with the asymmetry diminishing as r_1 increases. From (4.13), we see that the contact line displacements, ξ_1 and ξ_2 , are of different signs if the values of $\hat{h}_1(r)$ are of the same sign at both edges. This implies that the inner and outer contact lines evolve in opposite directions, which is characteristic of a varicose-like mode. In particular, the tendency of $g_1(\zeta)$ to become more symmetric as r_1 is increased is consistent with the limiting pure varicose mode, as we discuss further below. Further inspection of figure 10(a) shows that for small r_1 , the amplitude at the inner radius, $g_1(-1)$, is always larger than that at the outer one, $g_1(1)$, indicating that the perturbation is more significant at the regions characterized by larger azimuthal curvature. In figure 10(b) we show $g_2(\zeta)$, which is stable for the considered n . We note that the feature of the zigzag mode (i.e. different signs of $g_2(\zeta)$ at the inner and outer radius) is maintained even for large r_1 . On the other hand, the asymmetry of both g_1 and g_2 becomes more pronounced as r_1 decreases.

We now consider in more detail the change of character of the eigenfunctions as n is modified, and also discuss the appropriate limit of the ring problem to the straight

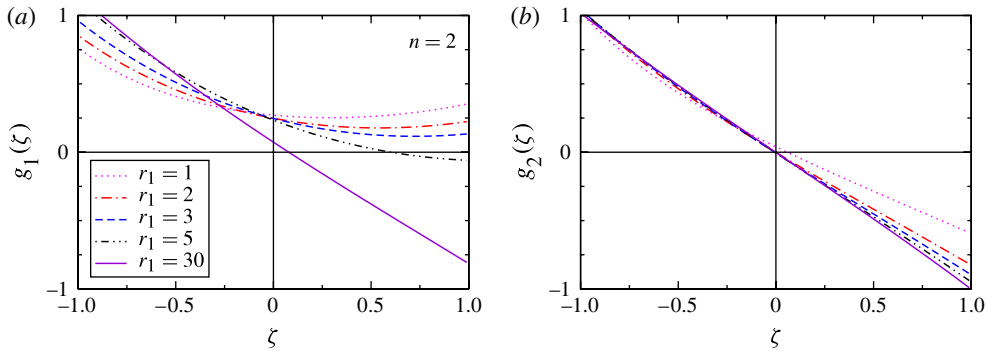


FIGURE 11. (Colour online) Eigenfunctions $g_1(\zeta)$ and $g_2(\zeta)$ for $n = 2$ and increasing values of r_1 . The rest of the parameters is as in figure 9.

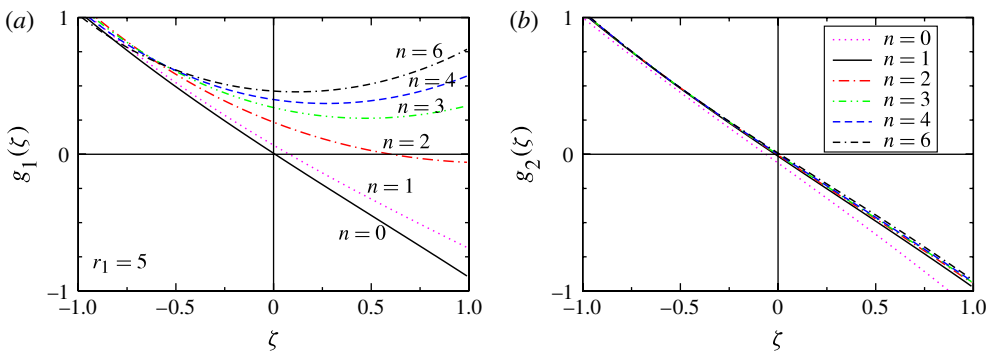


FIGURE 12. (Colour online) Eigenfunctions $g_1(\zeta)$ and $g_2(\zeta)$ for $r_1 = 5$ and decreasing values of n . The rest of the parameters are as in figure 9.

filament one. For this purpose, it is useful to point out that the behaviour of the eigenfunctions as $q \rightarrow 0$ can be analysed either for: (i) fixed n and $r_1 \rightarrow \infty$; or (ii) fixed r_1 and $n \rightarrow 0$ (since n has to be an integer, the latter limit is only formal); or (iii) both $n, r_1 \rightarrow \infty$ but with $n/r_1 \rightarrow 0$. In order to study case (i), we consider as an example $n = 2$ and show in figure 11 both g_1 and g_2 as r_1 increases. For moderate values of r_1 (of the order of the width w) we observe a varicose-like shape for g_1 and a zigzag-like shape for g_2 . However, for large r_1 , both modes tend to a purely zigzag mode in the limit $q \rightarrow 0$. Note that this is a different behaviour from the straight filament problem where (unstable) g_1 is of varicose type. Therefore, case (i) does not correspond to a straight filament. To help the discussion of case (ii), figure 12 shows the corresponding eigenfunctions for $r_1 = 5$, as n is varied. We see that the modes corresponding to $\omega_1(n)$ and $\omega_2(n)$ change their character along the dispersion curves. For example, g_1 is generally of the varicose type for moderate to large n (see figure 12a). However, its asymmetry increases as n decreases, acquiring a zigzag-like behaviour. Consequently, both g_1 and g_2 tend to the same zigzag mode for $n \rightarrow 0$ as in case (i). This discussion already suggests that case (iii) actually corresponds to the straight filament limit. This makes sense, since $r_1 \rightarrow \infty$ reduces the curvature, while taking $n \rightarrow \infty$ is consistent with the simultaneous increase of the system length.

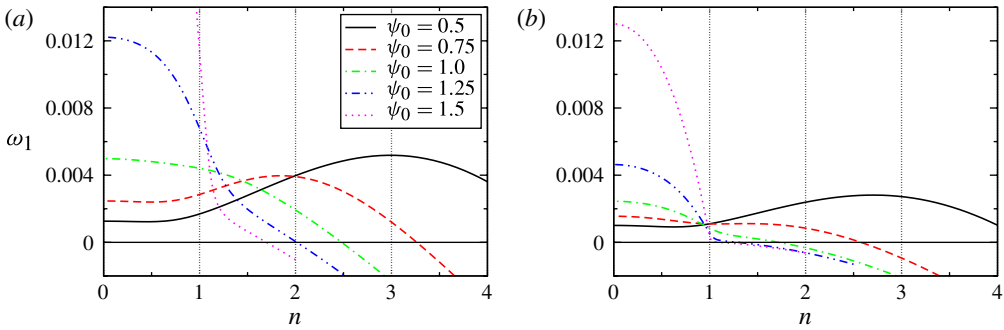


FIGURE 13. (Colour online) Largest eigenvalue, $\omega_1(n)$, for $r_m = 4$ and a set of values of the aspect ratio, ψ_0 : (a) without gravity ($G = 0$) and (b) with gravity ($G = 1$).

As expected, in this case we obtain g_1 as a pure varicose mode and g_2 as a pure zigzag mode for $q \rightarrow 0$, in agreement with the straight filament problem (Diez *et al.* 2012). This type of limit (where both $n, r_1 \rightarrow \infty$) is further discussed using analytical techniques in § 5.1 in the context of the study of the convergence of the marginal stability criterion of a ring to that of a straight filament.

4.3. Effect of the aspect ratio

Figure 13 shows the dispersion relations for different values of ψ_0 for given r_m , i.e. varying ring width w . Starting from small values of ψ_0 , we observe that for ψ_0 less than a certain value, $\psi_0^* \approx 0.85$, both the maximum growth rate, $\omega_{max} = \omega_1(n_{max})$, and its corresponding angular wavenumber, n_{max} , decrease as ψ_0 increases. For $\psi_0 > \psi_0^*$, the maximum jumps from $n_{max} \approx 2$ (recall that only integer values of n are physically admissible) to $n_{max} = 0$, and for larger ψ_0 the growth rate ω_{max} increases monotonically.

This behaviour is related to the change in tendency of the ring to collapse into a single central drop before breaking up into smaller drops (see § 5). It applies both with and without gravity. However, gravity reduces the growth rates and modifies the aspect ratio beyond which $n_{max} = 0$. In general, we observe that the geometric properties of the ring strongly affect the growth rates of the modes, which eventually will affect the final pattern of the instability. The combined effect of ψ_0 and r_m on the values of n_{max} and ω_{max} is studied below in § 5.2.

4.4. Effects of the contact angle

Figure 14(a) shows ω_1 normalized by $\tan^3 \theta_2$ for a set of angles and fixed radii r_1 and r_2 . The motivation for this normalization is the dependence of the coefficients of the operator \mathcal{L} on $H \sim H' \sim h_0^3$ far from the contact lines, i.e. where $h_0 \gg \ell$ (see (4.7)) and the fact that $h_0 \sim p \sim \tan \theta_2$ (see § 3). Although the simple scaling $\omega_1 \propto \tan^3 \theta_2$ is not strictly satisfied since it does not lead to a single curve in figure 14(a), we observe that the differences between curves are small. This indicates that any additional angular dependence is weak so that this scaling catches the main behaviour. Furthermore, if ℓ is reduced, the tendency to a universal curve becomes more apparent as shown in figure 14(b) for $\ell = 10^{-5}$.

As the positions of the maxima essentially do not change as θ_2 is varied, n_{max} remains practically unchanged. Therefore, the main effect of θ_2 is to determine the growth rates, which basically scale as $\tan^3 \theta_2$, while n_{max} remains fixed.

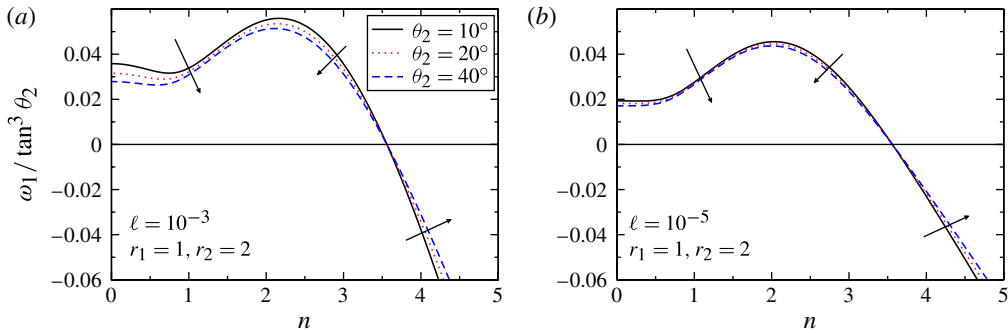


FIGURE 14. (Colour online) Normalized growth rates, $\omega_1(n)$, for $r_1 = 1$ and $r_2 = 2$ for different contact angles, θ_2 , and two different slip lengths: (a) $\ell = 10^{-3}$ and (b) $\ell = 10^{-5}$. The arrows indicate the effect of increasing θ_2 . The other parameters are as in figure 9.

5. Linear stability analysis predictions: ring breakup

As discussed in the previous section, the LSA shows that there exists a range of unstable wavenumbers. They eventually lead to a breakup of the ring into a number of drops in the nonlinear stages of instability development. Here we will assume that the LSA results can be extended to the nonlinear regime and discuss the resulting predictions. In the following two sections, we will further compare these predictions to the results obtained by using a quasi-static approach, § 6, and fully nonlinear simulations based on a disjoining pressure model, § 7.

Based on the LSA, an upper bound to the number of drops is given by the marginal mode with angular wavenumber n_c , characterized by zero growth rate. This marginal mode is analysed in detail in § 5.1. The modes near this bound are unlikely to be observed, however, due to their small growth rate. The mode n_{max} , corresponding to the maximum growth rate, provides a better estimate of the expected number of drops. Figure 13 tells us that $n_{max} = 0$ for ψ_0 larger than a certain value and, therefore, collapse is likely to occur for wide rings.

5.1. Marginal stability

In order to obtain the marginal stability criterion, we consider $n = n_c$, so that h_1 is time independent, see (4.1). Thus, (2.9) leads to

$$\nabla \cdot \left[h_0^2 (h_0 + \ell) \nabla (\nabla^2 - G) \hat{h}_1 \right] = 0, \tag{5.1}$$

since the equilibrium solution, h_0 , satisfies (3.2). After integrating and using the boundary conditions (2.4), we have

$$(\nabla^2 - G) \hat{h}_1 = 0, \tag{5.2}$$

where we have chosen the integration constant equal to zero, since a marginal perturbation does not affect the pressure of the base state. In the following we separate the study of the marginal solutions into two cases, depending on whether gravity is considered ($G = 1$) or not ($G = 0$).

The solution of (5.2) for $G = 0$ can be expressed as an eigenfunction of the form

$$h_1 = \left(Ar^{n_c} + \frac{B}{r^{n_c}} \right) \cos n_c \varphi. \tag{5.3}$$

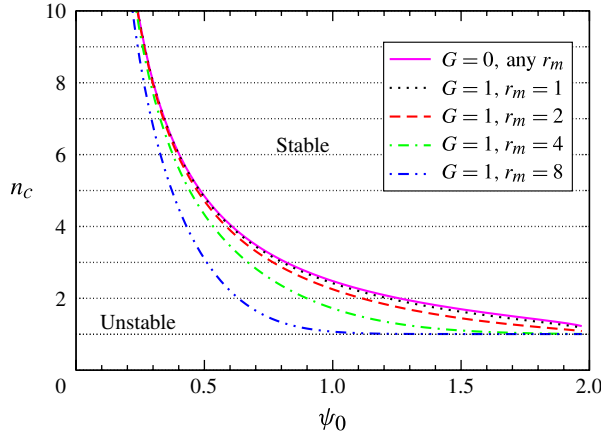


FIGURE 15. (Colour online) Critical value of n, n_c , as a function of the aspect ratio $\psi_0 = w/r_m$ for different ring sizes. Although only integer values n_c have physical meaning, we show a continuous curve to clearly distinguish the regions of stability and instability.

In order to satisfy the boundary conditions, we insert this expression into (4.10) and (4.11), and solve the system for A and B . The resulting condition for existence of a non-trivial solution is

$$\kappa^- \kappa^+ r_1 r_2 (r_1^{2n_c} - r_2^{2n_c}) + n_c^2 (r_2^{2n_c} - r_1^{2n_c}) + n_c (\kappa^- r_1 - \kappa^+ r_2) (r_1^{2n_c} + r_2^{2n_c}) = 0, \tag{5.4}$$

which yields n_c , which is independent of the contact angles, θ_1 and θ_2 . Alternatively, by writing (5.4) in terms of r_m and ψ_0 , we observe that n_c is independent of r_m since, by using (3.8) and (3.10) we can write

$$\kappa^- = f_1(\psi_0)/r_m, \quad \kappa^+ = f_2(\psi_0)/r_m \quad \text{for } G = 0, \tag{5.5}$$

where f_1 and f_2 are known functions of ψ_0 . Consequently, only the ring's aspect ratio determines the region of stability. Figure 15 shows this result, where the solid line for $G = 0$ defines the stability regions for any r_m .

To compare (5.4) with the results obtained for a straight infinite filament on a horizontal plane, we consider the limit $r_m, n_c \rightarrow \infty$. It is appropriate to define the marginal wavenumber as $q_c = n_c/r_m$. In this limit $\kappa^\pm \rightarrow \kappa$ and we find

$$-2\kappa q_c \cosh q_c w + (\kappa^2 + q_c^2) \sinh q_c w = 0, \tag{5.6}$$

which is coincident with the results reported in Diez *et al.* (2012).

When gravity is considered ($G = 1$), the solutions of (5.2) are of the form

$$h_1 = A I_{n_c}(r) + B K_{n_c}(r). \tag{5.7}$$

As done previously in the non-gravity case, we replace this expression into the boundary conditions now given by (4.10) and (4.11). A non-trivial solution for n_c can be found provided that the condition

$$\frac{I_{n_c-1}(r_2) - A_2 I_{n_c}(r_2)}{K_{n_c-1}(r_2) + A_2 K_{n_c}(r_2)} = \frac{I_{n_c-1}(r_1) - A_1 I_{n_c}(r_1)}{K_{n_c-1}(r_1) + A_1 K_{n_c}(r_1)} \tag{5.8}$$

is satisfied, where

$$A_1 = \kappa^- + \frac{n_c}{r_1}, \quad A_2 = \kappa^+ + \frac{n_c}{r_2}. \tag{5.9}$$

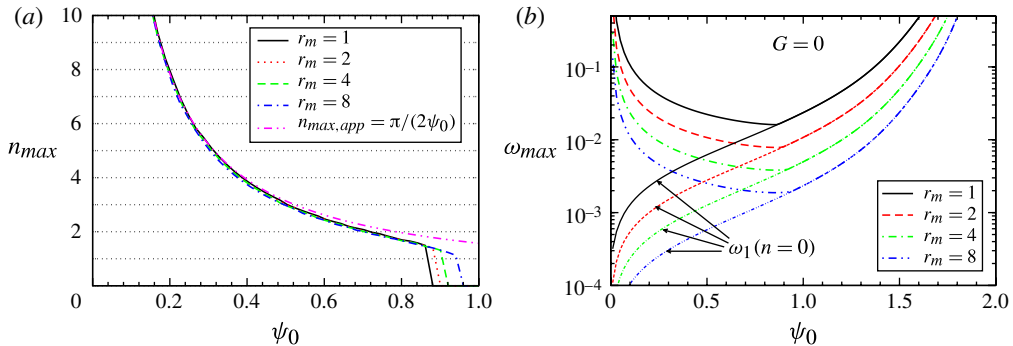


FIGURE 16. (Colour online) Dependence of (a) n_{max} (expected number of drops) and (b) $\omega_{max} = \omega_1(n_{max})$ on the initial aspect ratio ψ_0 for $G = 0$ and several values of r_m . The thin lines in (b) show ω_1 for $n = 0$.

Thus, (5.8) and (5.9) allow us to obtain n_c for $G = 1$. In contrast to the $G = 0$ case, n_c now depends on both ψ_0 and r_m . Nevertheless, the independence of n_c on both θ_1 and θ_2 still remains as in the case $G = 0$ (cf. figure 14), since both κ^- and κ^+ are contact angle independent (see (4.12)).

Figure 15 gives the corresponding results, showing that the presence of gravity always has a stabilizing effect since the stable region increases for $G = 1$. This stabilization becomes more pronounced for larger r_m , as expected due to the flattening of the static thickness profile in the presence of gravity, see figure 5. Since n_c represents the maximum possible number of drops, we can conclude that for large r_m and $\psi_0 > 1$, only one (central) drop is expected to form.

5.2. The mode of maximum growth

Now we focus on the predictions of the LSA regarding the expected number of drops, approximated by $n = n_{max}$, for which the growth rate is maximum. Figure 16(a) shows n_{max} when gravity is ignored. For small ψ_0 , n_{max} practically does not depend on r_m , similarly to what was found for n_c . For ψ_0 greater than a certain critical value, $\psi_0^* \approx 0.85$, n_{max} decreases abruptly and jumps from $n_{max} \gtrsim 1$ to $n_{max} = 0$. This effect is due to the fact that the growth rates for $n = 0, 1, 2$ become very close to each other for $\psi_0 \approx \psi_0^*$, as illustrated in figure 13(a). Physically, this means that a ring could evolve with almost the same likelihood to either a single centred drop ($n = 0$), a single off-centred drop ($n = 1$) or two drops ($n = 2$) for $0.75 \lesssim \psi_0 \lesssim 1$; a more thorough analysis of the predictions regarding the final number of drops is given in § 6. The abrupt transition from $n_{max} > 1$ to $n_{max} = 0$ at ψ_0^* is correlated with the change of dependence of ω_{max} on ψ_0 . Figure 16(b) illustrates this effect, showing that ω_{max} changes from a decreasing to an increasing function of ψ_0 . The critical value, ψ_0^* , where this change takes place, increases slightly with r_m . We note that although the mean radius of the ring, r_m , does not influence the LSA prediction for the expected number of drops, n_{max} , it strongly affects the growth rate of the instability that leads to that pattern.

Figure 17 shows that a similar picture is obtained when gravity is included ($G = 1$). The main difference compared with $G = 0$ is that ψ_0^* is smaller for the same r_m , and that it noticeably decreases with r_m . For sufficiently large r_m , n_{max} may fall down from $n_{max} \geq 2$ directly to $n_{max} = 0$, so that the likelihood of having an off-centred

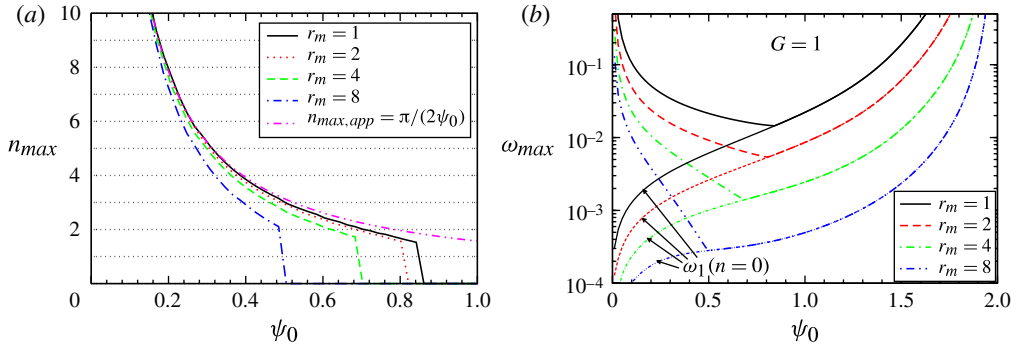


FIGURE 17. (Colour online) Dependence of (a) n_{max} (expected number of drops) and (b) $\omega_{max} = \omega_1(n_{max})$ on the initial aspect ratio ψ_0 for $G = 1$ and several values of r_m . The thin lines in (b) show ω_1 for $n = 0$.

drop ($n = 1$) is small. For both cases (with and without gravity), for large r_m and $\psi_0 > 1$, a single central drop is expected to form.

Figures 16(a) and 17(a) also show the curve

$$n_{max,app} = \pi / (2\psi_0) \approx 1.57r_m/w, \tag{5.10}$$

as an attempt to approximate n_{max} for $\psi_0 < 1$. The accuracy of the approximation is very good in particular for small ψ_0 . This suggests that the wavelength (i.e. the average distance between drops along the perimeter) is given by

$$\lambda = \frac{2\pi r_m}{n_{max,app}} = 4w, \tag{5.11}$$

independently of r_m . In fact, the value predicted for a straight filament (i.e. when the azimuthal curvature effects are not present) is very close to this value, with a weak dependence on the contact angle (Diez *et al.* 2009, 2012), see also §4.4. In a different setting, recent experiments by Pairam & Fernández-Nieves (2009) carried out with rings of glycerin immersed in a liquid phase (silicon oil) yield the relation $n_{max} \approx 1.14r_m/w$, which is comparable to the prediction (5.10) in spite of the differences between their experiments and the present problem. It should be also mentioned that the older experiments with mercury rings falling down on a substrate by Worthington (1879) yield $n_{max} = (2\pi\sqrt{2}/6.1)r_m/w \approx 1.45r_m/w$, in good agreement with (5.10).

In order to analyse the competition between and breakup of the ring, we introduce here the collapse and breakup times, t_c and t_b , respectively. When only the mode $n = 0$ is present, the ring evolves in a axisymmetric fashion, leading to the closure of the inner hole (collapse) and the subsequent formation of a single central drop. Assuming that the LSA approach can be extended throughout the evolution, the collapse time, t_c , can be roughly estimated as

$$t_c = \frac{1}{\omega_{1,0}} \ln \left(\frac{r_1}{\epsilon} \right), \tag{5.12}$$

where $\omega_{1,0} = \omega_1(n = 0)$ is assumed to be time independent and ϵ is the initial amplitude of the perturbation. Similarly, we define the time it takes a certain mode $n > 0$ to produce a pinch-off of the ring as the breakup time, t_b . Assuming that the

ring width decreases exponentially with time, t_b can be estimated as

$$t_b = \frac{1}{\omega_{1,n}} \ln \left(\frac{w}{\epsilon} \right), \tag{5.13}$$

where $\omega_{1,n} = \omega_1(n > 0)$.

The comparison of t_b and t_c gives an idea whether a ring would breakup or collapse. Clearly, one can question the assumption that the instantaneous growth rate of the modes remains equal to its initial value for varying radius and width as the ring evolves. In the next section, we develop a more elaborated quasi-static model based on a WKB (Wentzel–Kramers–Brillouin) type of analysis to obtain better predictions for both t_c and t_b .

6. Quasi-static modelling

So far, we have considered a static ring and its stability. Now we extend our approach to consider an evolving ring which slowly collapses, or breaks up into drops. The concept of ‘slow’ evolution can be related to a quasi-static process, where the instantaneous thickness profile is similar to the static one for the corresponding values of ψ_0 and r_m . A similar approach has been considered elsewhere, see e.g. González *et al.* (2004) for a flow of a fluid down an incline or Münch & Wagner (2005) for an analysis of a dewetting process. The assumption of quasi-static behaviour will be tested and confirmed in § 7.

For brevity, we restrict to the case $G = 0$. To begin with, we write the equations of motion for the perturbed inner and outer radii as (see also (4.2) and (4.3))

$$R_1(\varphi, t) = r_1 + \epsilon \xi_1 \cos(n\varphi) F(n, t), \tag{6.1}$$

$$R_2(\varphi, t) = r_2 + \epsilon \xi_2 \cos(n\varphi) F(n, t), \tag{6.2}$$

where $F(n, t) = \exp[\int_0^t \omega_1(n, t') dt']$, and $\omega_1(n, t)$ is the growth rate of mode n as given by the LSA of a ring of instantaneous radii $R_1(\varphi, t)$ and $R_2(\varphi, t)$; recall that r_1 and r_2 stand for the initial values of the unperturbed (φ -independent) ring radii. We will now study the collapse and breakup processes separately.

6.1. Radial collapse

We first analyse the axisymmetric convergent flow of the ring for $n = 0$ so that R_1 and R_2 are φ -independent. The above definitions lead to the following expression for the instantaneous aspect ratio,

$$\psi(t) = 2 \frac{R_2(t) - R_1(t)}{R_2(t) + R_1(t)} = \frac{w_c(t)}{R_m(t)}, \tag{6.3}$$

where

$$w_c(t) = w + \delta w_c F(0, t), \quad R_m(t) = \frac{R_1(t) + R_2(t)}{2} = r_m + \delta r_m F(0, t), \tag{6.4}$$

are the perturbed width and mean radius of the ring (subscript ‘c’ stands for ‘collapse’). Also, $\delta w_c = \epsilon(\xi_2 - \xi_1)|_{n=0}$ and $\delta r_m = (\epsilon/2)(\xi_1 + \xi_2)|_{n=0}$. The growth rate $\omega_1(0, t)$ is a function of both the instantaneous aspect ratio, $\psi(t)$, and of the mean radius, $R_m(t)$. Since the evolution is performed for a fixed volume, V , $R_m(t)$ is a

function of $\psi(t)$ as (see (3.19))

$$R_m(t) = \left(\frac{\pi\psi(t)[\psi(t) + 2]}{V} \frac{[\psi(t)^2 + 4] \tanh^{-1}(\psi(t)/2) - 2\psi(t)}{2[\psi(t) + 2]^2 \tanh^{-1}(\psi(t)/2) - 4\psi(t)} \tan \theta_2 \right)^{-1/3}. \tag{6.5}$$

Thus, we can simply write $\omega_1(0, t) = \Omega_c(\psi(t))$. By taking a derivative of (6.3) and replacing $F'(0, t) = \Omega_c(\psi(t))F(0, t)$, we have

$$r_m \frac{d\psi}{dt} = F(0, t) \left[\Omega_c(\psi(t)) (\delta w_c - \psi \delta r_m) - \frac{d\psi}{dt} \delta r_m \right]. \tag{6.6}$$

Using (6.3) to eliminate $F(0, t)$, we obtain the equation for evolution of ψ

$$\frac{d\psi}{dt} = -\Omega_c(\psi(t)) \frac{\psi - \Delta_c}{\psi_0 - \Delta_c} (\psi - \psi_0), \tag{6.7}$$

where $\Delta_c = \delta w_c / \delta r_m$ and $\psi_0 = w / r_m$ is the initial ($t = 0$) aspect ratio of the unperturbed ring (to be distinguished from the initial aspect ratio of the unperturbed ring introduced below). Integrating, we have the implicit relationship $t(\psi)$ for the radially convergent flow as

$$t(\psi) = \int_{\psi(0)}^{\psi} \frac{\psi_0 - \Delta_c}{\Omega_c(\psi(t))(\psi - \Delta_c)(\psi - \psi_0)} d\psi, \tag{6.8}$$

where the lower limit corresponds to the (perturbed) aspect ratio at $t = 0$. Following (6.3), this quantity can be written as

$$\psi(0) = \frac{w + \delta w_c}{r_m + \delta r_m} \approx \psi_0 - \psi_0 \frac{\delta r_m}{r_m} + \frac{\delta w_c}{r_m} \tag{6.9}$$

correct to the first order in $\delta r_m / r_m$.

Since the ring volume is kept constant during the evolution, from (3.19) we have

$$3 \frac{\delta r_m}{r_m} + \frac{f(\psi_0)}{f'(\psi_0)} \delta \psi = 0, \tag{6.10}$$

where $\delta \psi$ is given by (6.9) as

$$\delta \psi = \psi(0) - \psi_0 \approx \frac{\delta r_m}{r_m} (\Delta_c - \psi_0). \tag{6.11}$$

By replacing into (6.10) we obtain

$$\Delta_c = \psi_0 - \frac{3f'(\psi_0)}{f(\psi_0)}. \tag{6.12}$$

Note that in order to trigger the collapse, one expects $\delta r_m < 0$, i.e. it is required that both radial perturbations ξ_1 and ξ_2 are negative. The LSA calculations using (4.13) confirm that this is the case. In addition, $f'(\psi_0) > 0$ for $0 < \psi_0 < 2$, and consequently $\delta \psi > 0$, i.e. the net effect of the perturbations at the contact lines for the mode $n = 0$ is to increase the aspect ratio. Finally, for a given ψ_0 the integral in (6.8) can be calculated by using the instantaneous growth rates as obtained from the LSA developed in §4. Thus, the collapse time is given by $t_c = t(\psi = 2)$.

We now choose a fixed volume, and specify $r_m = 1$ and $\psi_0 = 0.5$, giving $V = 0.16$; also we use $\epsilon = 10^{-3}$. Figure 18(a) shows t_c as function of ψ_0 ((blue) solid line

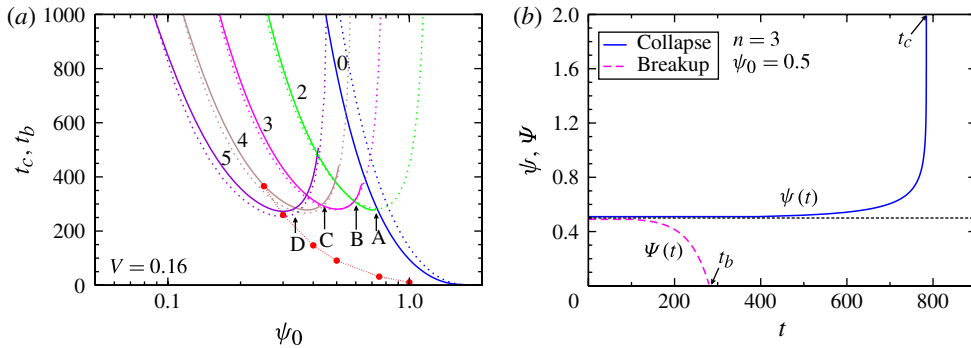


FIGURE 18. (Colour online) (a) Collapse and breakup times, t_c and t_b , obtained by using the quasi-static approximation (solid lines) versus the initial aspect ratio of the ring, ψ_0 , for a fixed volume $V = 0.16$. The numbers indicate the corresponding n modes. The dotted lines are the times obtained from the LSA as given by (5.12) and (5.13). The full circles show the collapse times calculated using disjoining pressure simulations as described in § 7. (b) Time evolutions of the global aspect ratio, $\psi(t)$, and the local aspect ratio, $\Psi(t)$, for $n = 3$. The initial aspect ratio of the ring is $\psi_0 = 0.5$ and the average radius $r_m = 1$, for the same volume as in (a). We use $\theta_0 = 30^\circ$, $\ell = 10^{-3}$ and $G = 0$.

marked by 0); note that we use the value of r_m that keeps the volume constant. For comparison, we also plot the collapse time as obtained using the LSA as given by (5.12), which yields slightly larger values of t_c . The reason for the difference can be seen in figure 18(b), which shows that the growth rate of the $n = 0$ mode (see the (blue) solid line), does not remain constant, as assumed by the LSA, but it instead increases as the collapse proceeds. For the present choice of parameters, this increase is concentrated near the very end of the collapse. For smaller values of ψ_0 , the increase extends for longer periods and yields larger departures of t_c from the LSA results.

6.2. Breakup of the ring

Now we consider a quasi-static approximation with the goal of estimating the breakup times for various angular wavenumbers. We consider a single value of the azimuthal angle, φ , such that $|\cos(n\varphi)| = 1$, i.e. we concentrate at a neck of the mode n which evolves towards a pinch-off.

We consider the evolution of the width of the ring concomitant with the radial convergence described previously. Therefore, the ring width is being perturbed simultaneously by both the mode $n = 0$, which triggers the ring collapse, and by a mode with $n > 0$, which tends to produce a breakup. Thus, we write the resultant ring width as

$$w_n(t) = w_c(t) - \delta w_n F(n, t), \quad (6.13)$$

where $\delta w_n = \epsilon(\xi_2 - \xi_1)|_{n>0}$. At breakup, we have $w_n(t_b) = 0$, so that (6.13) leads to

$$\ln \frac{w_c(t_b)}{\delta w_n} = \int_0^{t_b} \Omega_n(\psi(t)) dt, \quad (6.14)$$

where $\Omega_n(\psi(t)) = \omega_1(n, t)$ is the growth rate for the instantaneous value of the global aspect ratio $\psi(t)$ of the ring.

Equation (6.14) implicitly yields the breakup time, t_b , for the mode n , and it is solved simultaneously with (6.8). As an example, figure 18(b) shows the evolution of the local aspect ratio $\Psi(t) = w_n(t)/R_m(t)$ for the mode $n = 3$ (dashed line), which depicts a typical case where the ring breaks up due to the presence of this mode. As before, we use $\epsilon = 10^{-3}$ for this and for all of the other modes considered below.

Figure 18(a) shows the values of t_b versus ψ_0 for the first few modes (solid lines). The dotted lines correspond to (5.13). Unlike the comparison made for t_c , the breakup times obtained using the LSA are smaller than those given by the quasi-static method. The reason is that $\omega_1(n, t)$ decreases as ψ_0 increases (see e.g. figure 13a) and therefore the instantaneous growth rates obtained by the quasi-static method are smaller. Note that the mode $n = 1$ is not plotted here since $t_b|_{n=1} > t_c$ and is out of the time range shown in figure 18(a). This suggests that this mode, which would imply a single breakup and formation of an off-centre single drop, is very unlikely to be seen in an actual flow.

Note that the breakup times given by the quasi-static method can be calculated only up to a certain maximum value of ψ_0 , depending on the value of n . This result points out that the mode n does not have time to break up the ring before it collapses. This is another difference compared with the LSA, which cannot show this effect since it considers the collapse and breakup process independently, and not coupled as done in quasi-static approach to describe more accurately the actual flow.

We observe that the most likely breakup mode, which is that with the lowest t_b , varies depending on the value of ψ_0 in the ranges marked in figure 18(a) by A, B, C and D. Thus, we have that the mode $n = 2$, i.e. the formation of two drops, is likely to occur for $\psi_{0,B} < \psi_0 < \psi_{0,A}$, $n = 3$ for $\psi_{0,C} < \psi_0 < \psi_{0,B}$, and so on for larger n .

Note that, in principle, one could think of the approximations given by (5.12) and (5.13) as underestimates of t_c and t_b , since the exponential behaviour assumed for the whole process should lead to faster velocities compared to those expected in the later nonlinear stages (where some type of saturation occurs). When comparing with the quasi-static results, we see that the LSA indeed underestimates t_b , but it also overestimates the collapse times, t_c . This overestimate is due to the fact that the growth rate of the initial aspect ratio (which is kept constant under the LSA) is smaller than those for later (larger) aspect ratios considered in the quasi-static method (see figure 16).

7. Comparison with disjoining pressure model

The condition of partial wettability is also treated in the literature by the introduction of long range intermolecular forces, such as those of van der Waals (vdW) type. This is usually done by including a new term at the left-hand side of (2.2) in the form, see Diez & Kondic (2007) for a review,

$$K \frac{\partial}{\partial x} \left(h^3 f'(h) \frac{\partial h}{\partial x} \right), \quad (7.1)$$

and by setting ℓ to zero. Here, $f(h)$ stands for the conjoining–disjoining pressure as

$$f(h) = \left(\frac{h_*}{h} \right)^3 - \left(\frac{h_*}{h} \right)^2, \quad (7.2)$$

where h_* is the equilibrium thickness of a flat film subject only to this pressure. Thus, it corresponds to the thickness of the film ahead of the contact lines, extending

(mathematically) to infinity. The (dimensionless) constant K is given by

$$K = \frac{2(1 - \cos \theta_0)}{h_*}, \quad (7.3)$$

where $\theta_0 \approx \tan \theta_0$ is the asymptotic slope of the free surface at the inflection point of $h(x)$.

Before proceeding with a comparison between the slip and disjoining pressure models, it is important to point out that a full quantitative agreement should not be expected, since there are significant differences between the models. The first is that slip model discussed so far concentrates on a configuration where contact angles hysteresis is crucial: the analysis relies on the presence of hysteresis for the existence of a static solution. The disjoining pressure as presented here does not include the effect of contact angle hysteresis, a static solution does not exist and the ring inevitably converges towards the centre due to the differences in pressures associated with the azimuthal curvature of the contact lines. Note that introducing contact angle hysteresis under disjoining pressure approach is complicated due to the global character of the additional pressure field. This problem is not present under the slip model where different contact angles can be imposed locally. The second difference is that the slip model was considered on the level of LSA of static or quasi-static configurations. These (quasi-)static configurations do not exist within the disjoining pressure model and therefore we need to resort to (nonlinear) simulations to understand the dynamics. Owing to these differences, only qualitative comparison is expected. However, we note that in the recent comparison of the models by Savva & Kalliadasis (2011), it was found that in many cases of interest the agreement between the results extends even beyond the quasi-static regime considered here.

We report here the results obtained by solving (2.2) with the addition of the disjoining pressure term (7.1), by employing a procedure based on the alternating direction implicit (ADI) method which is described in detail elsewhere, see Lin, Kondic & Filippov (2012). This approach turns out to be significantly more efficient compared with the fully implicit discretization (see Diez & Kondic 2002; Diez *et al.* 2009). To ensure accuracy, we have carried out selected simulations using both methods and obtained indistinguishable results. These non-axisymmetric simulations are carried out in a square computational domain divided into cells of size $\Delta x \times \Delta y$, and the domain size is $1.1r_2$. We impose no-flow boundary conditions along the domain boundaries, by setting both the first and third derivatives of $h(x, y, t)$ to zero there. For brevity, we restrict the focus to vanishing gravity case ($G = 0$).

7.1. Axisymmetric rings

We first consider the time evolution within the disjoining pressure model by axisymmetric simulations, where we consider only the cross-section of a ring. Figure 19 shows the thickness profiles at different times, using as an initial condition the static solution obtained in § 3.1. Here we use $\Delta x = h_*$, which is sufficient for numerical convergence. For each time, we compare these profiles with the static ones calculated using the instantaneous values of r_1 and r_2 as given by the disjoining pressure simulations and conserving the initial ring volume. We find that the difference between the instantaneous values of θ_2 (the angle at the outer radius) and θ_0 is small, less than 5%. This agreement between the static profiles and the instantaneous thickness profiles as given by the disjoining pressure model strongly suggests that the evolution can be considered as quasi-static, although a careful comparison of the profiles near the closure (not shown in detail in the figure) shows that the difference

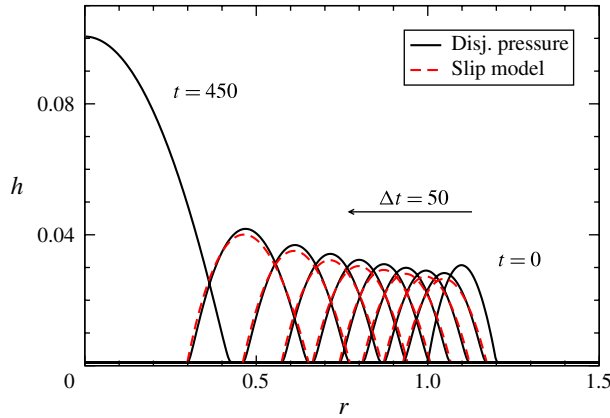


FIGURE 19. (Colour online) Numerical simulation of the evolution of a ring specified by $r_1 = 1$, $r_2 = 1.2$ ($r_m = 1.1$, $\psi_0 = 0.182$) and $\theta_2 = 30^\circ$ (solid lines) using the disjoining pressure model with $\theta_0 = 30^\circ$ and $h_* = 10^{-3}$ (see (7.2) and (7.3)). The dashed lines correspond to the static solutions obtained using the slip model and lifted by h_* . The profiles were calculated using the instantaneous values of r_1, r_2 as given by simulations based on the disjoining pressure model, and using the value of θ_2 obtained from volume conservation.

between both types of profiles increases there. The main difference between the results of the two models has to do with the speed of collapse: as shown in figure 18, the collapse time, t_c , is typically shorter under the considered disjoining pressure model. This is particularly obvious for large ψ_0 , suggesting that for the rings characterized by large aspect ratio we may expect differences in the non-axisymmetric cases as well. As pointed out at the beginning of the section, these differences between the results of the two models are expected.

7.2. Non-axisymmetric rings

In the following, we discuss the time evolution of the rings by solving the complete governing equation without assuming axisymmetric flow. The initial profile, $h_0(x, y, 0)$, is given by (3.5)–(3.11), lifted by h_* . We perturb this profile by a varicose mode which radially shifts $h_0(x, y, 0)$ as follows

$$h_{pert}(r, \phi, 0) = \begin{cases} h_0(r - \delta(\phi)), & r > r_m \\ h_0(r + \delta(\phi)), & r < r_m \end{cases} \quad (7.4)$$

where $\delta(\phi)$ is an imposed shift, and we interpolate the region around r_m to ensure smoothness.

In order to compare the growth rates obtained from the disjoining pressure model with those predicted by the LSA based on the slip model (called just ‘LSA’ in what follows for brevity), we consider a single mode perturbation

$$\delta(\phi) = A_0 \cos(n\phi), \quad (7.5)$$

for a single angular wavenumber n with radial amplitude A_0 . Figure 20 shows the time evolution of the corresponding thickness amplitude of the ring (solid line) for $n = n_{max} = 8$ and $A_0 = 0.01$ applied to the case shown in figure 19. This amplitude is obtained as the difference between the maximum thickness of the ring in axisymmetric and non-axisymmetric simulations at $\phi = 2\pi/n$. This approach allows us to quantify

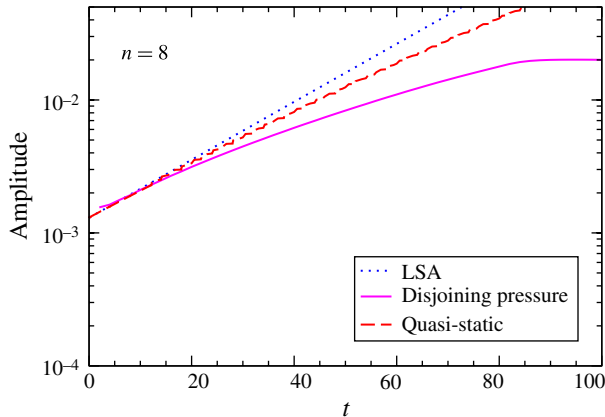


FIGURE 20. (Colour online) Single-mode perturbation: amplitude of the thickness perturbation as a function of time for $r_1 = 1$, $r_2 = 1.2$, $\theta_0 = 30^\circ$ and $h_* = 10^{-3}$ as given by the non-axisymmetric disjoining pressure model (solid curve). The slope of the dotted line corresponds to the growth rate, ω_1 , given by LSA for $n = 8$ with slip length $\ell = 10^{-3}$ ($\omega_1 = 0.0502$), and the dashed line to the quasi-static method.

the evolution of the azimuthal perturbation of the (quasi-static) axisymmetric base solution. Since, as shown in § 7.1, the axisymmetric thickness profiles obtained for the disjoining pressure model are remarkably similar to the static base solution obtained using the slip model, one can compare the results of the LSA and quasi-static approach for the slip model with those of the disjoining pressure model for non-axisymmetric modes. The dotted line in figure 20 shows the exponential time evolution of a perturbation with the growth rate as given by the LSA using $n = 8$. For early times, the agreement between the LSA and the disjoining pressure model is quite satisfactory. We also show a quasi-static calculation (dashed line) which takes into account the progressive change of the aspect ratio, ψ . This model extends the agreement to longer times, and shows the decaying trend of the growth rate. Naturally, this agreement does not extend to the late times when axisymmetric calculations approach a final collapse and non-axisymmetric evolution tends to a breakup.

In any physical experiment, one expects the presence of white noise which may influence the evolution. While the noise influences both the initial configuration and the evolution that follows, we expect that a good insight can be reached by considering its influence on the initial shape of a ring only. The perturbations due to noise can be expanded into an infinite Fourier series, which we approximate here by a superposition of a finite number, N , of modes with random amplitudes, as follows

$$\delta(\phi) = \sum_{n=1}^N A_n \cos(n\phi), \quad (7.6)$$

where A_n are random amplitudes such that $|A_n| < A_{max}$. Here, we set $N = 50$, $A_{max} = 10^{-3}$ and use $\Delta x = \Delta y = 5 \times 10^{-3}$. While full numerical convergence is difficult to achieve for these non-axisymmetric simulations due to high computational cost, our previous results using similar method (see Diez & Kondic 2007; Diez *et al.* 2009, 2012) suggest that this level of resolution is sufficient to accurately capture the dynamics.

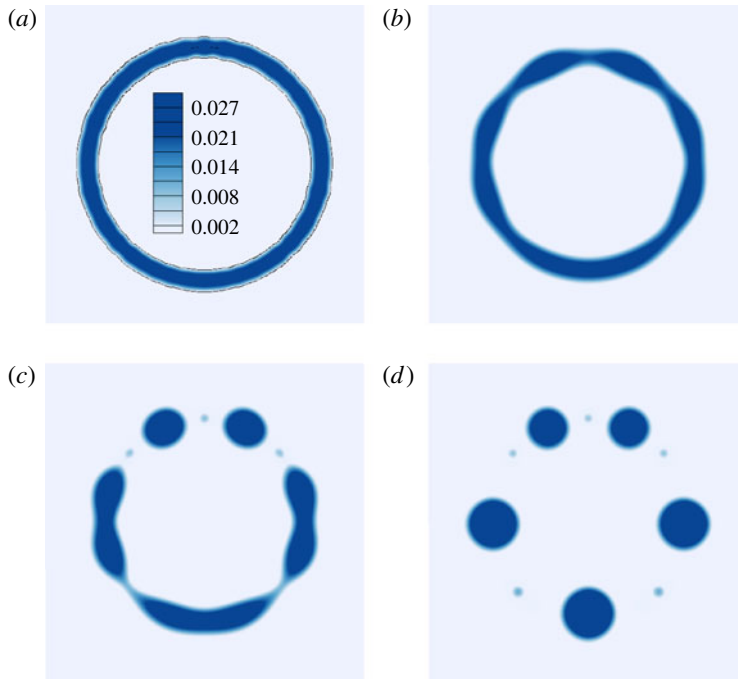


FIGURE 21. (Colour online) Multiple mode perturbation: snapshots from the disjoining pressure model of a ring with $r_1 = 1$ and $r_2 = 1.2$ ($\psi_0 = 0.182$) with $\theta_0 = 30^\circ$ and $h_* = 10^{-5}$. The initial condition was perturbed by a set of azimuthal varicose modes with random amplitudes as given by (7.4) and (7.6). The LSA under the slip model yields $n_{max} = 16.8$: (a) $t = 0$; (b) $t = 100$; (c) $t = 150$; (d) $t = 250$.

The question now is to which degree the computed dynamics compares with the LSA results obtained using the slip model. To discuss this question, we first consider initially small aspect ratios, ψ_0 , where we expect breakup, and then consider larger ψ_0 , where competition between collapse and breakup is expected. Based on the discussion in § 7.1, better agreement is expected for smaller ψ_0 .

Figure 21 shows snapshots for the ring with $r_2 = 1.2$ ($\psi_0 = 0.182$) evolving after being perturbed by the superposition of modes specified above. The LSA here gives $n_{max} = 8.7$. While a corresponding number of modes appear to be dominant for early times (see figure 21b), for longer times, as the ring converges towards the centre, some breakups predicted by the LSA do not take place and the final number of drops is five. A similar trend (of smaller number of drops) was also noticed in the comparison with experimental results involving liquid metal rings (Wu *et al.* 2011).

Figure 22 shows the comparison for $r_2 = 1.1$ ($\psi_0 = 0.095$) where 16 drops are formed; here $n_{max} = 16.8$. In general, we observe that for smaller values of ψ_0 the agreement of the number of resulting drops between the disjoining pressure and the slip model becomes very good. We also note that the simulation shown in figure 21 leads to the formation of satellite droplets, which are in some cases also observed in physical experiments, see González *et al.* (2007), while the simulations in figure 22 do not lead to satellite droplets; this detail of the breakup process deserves further consideration, which is however out of the scope of the present paper.

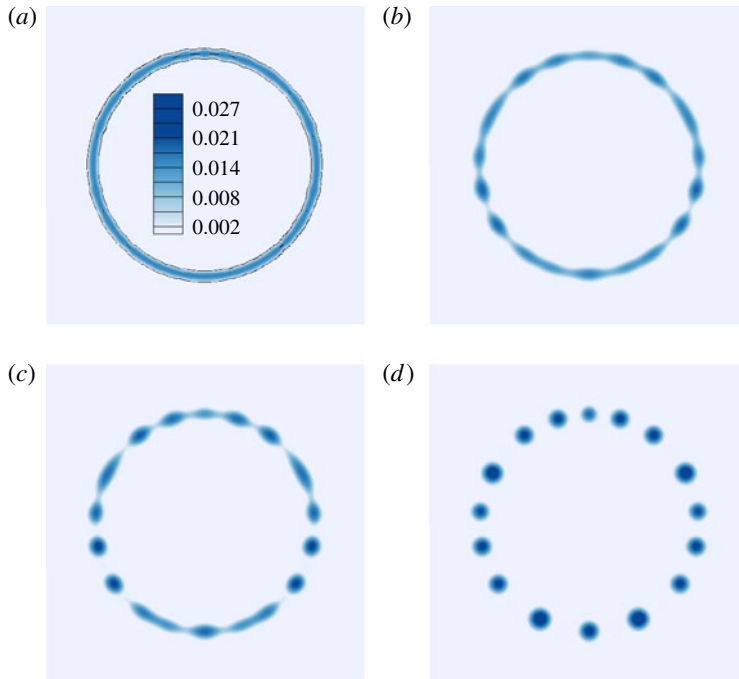


FIGURE 22. (Colour online) Similar to figure 21, but with $r_2 = 1.1$ ($\psi_0 = 0.095$). The LSA under the slip model yields $n_{max} = 16.8$: (a) $t = 0$; (b) $t = 40$; (c) $t = 50$; (d) $t = 100$.

For larger ψ_0 , we expect more significant differences between the disjoining pressure and the slip model, in particular due to the shorter collapse times of axisymmetric profiles in the former case (see figure 18). These shorter collapse times are expected to lead to collapse in the case where slip model may predict breakup. Simulations (not shown here for brevity) show that this is indeed the case. For example, the case $r_2 = 1.4$ ($\psi_0 = 0.33$) and the other parameters as in figure 21 leads to collapse, while the LSA predicts breakup. Additional parameters come into play here as well: for example, the same simulation with larger initial perturbation amplitude leads to a breakup, showing that the details of the setup of simulations (or physical experiments) may lead to different outcomes in this transitional range of parameters.

8. Summary and conclusions

In this paper we are concerned with a liquid ring on a horizontal surface under partial wetting conditions with and without gravity effects. We find that there exist static solutions describing the ring shape, whose inner and outer contact angles, θ_1 and θ_2 , respectively, are different. Physically, the existence of a static ring on a homogeneous substrate requires that the fluid–solid interaction includes hysteretic effects. This feature is analogous to the problem of a drop or a filament on an inclined plane as considered recently by Diez *et al.* (2012).

The ring stability is studied by analysing small perturbations of the fluid thickness as well as of the contact lines. The eigenvalue problem derived from the linearization of the perturbed equations is solved by using a Chebyshev pseudo-spectral method. In

this method, we choose a convenient set of basis functions that automatically satisfies the boundary conditions at the contact lines. This approach leads to a fast and accurate numerical scheme.

It is found that the limiting case of a large radius ring with a fixed width is consistent with that of a straight filament of infinite length. A distinctive property of the ring evolution is that the growth rate of the $n = 0$ axisymmetric mode is not equal to zero due to the lack of translational invariance. The mode $n = 0$ plays a fundamental role in determining whether a ring collapses into a central drop, or breaks up into multiple drops.

The LSA shows that the marginal stability angular wavenumber, n_c does not depend on the contact angles and furthermore, that the dependence of the mode of maximum growth, n_{max} , on the contact angles is very weak. However, the growth rates scale with the contact angle approximately as $\tan^3\theta_2$, and this scaling becomes more accurate for smaller values of slip length, ℓ . Therefore, only the internal and external radii are left as the main parameters on which the instability process can depend upon. Further insight into the problem can be reached by considering the mean radius, r_m , and the aspect ratio, $\psi_0 = w/r_m$, as the variables describing the ring evolution. When gravity effects are negligible, a remarkable result is that n_c does not depend on r_m , and it is a decreasing function of ψ_0 . When gravity effects are considered, the dependence on r_m is significant only for some intermediate range of ψ_0 .

Nonlinear stages of evolution lead to either collapse or breakup of a ring. Assuming that the LSA predictions can be extended to these stages, we estimate the expected number of drops by n_{max} . In general, we find that n_{max} is mostly influenced by the aspect ratio, ψ_0 . Large ψ_0 lead to a central collapse, and breakup into drops results for small ψ_0 , say $\psi_0 < 0.4$ (cf. figures 16 and 17). In the intermediate region of ψ_0 , gravity decreases the expected number of drops by an amount that depends on the mean ring radius. We find that the results regarding dependence of the number of drops on the aspect ratio of a ring are in good agreement with existing experimental data.

In order to extend the validity of our results, we develop a quasi-static approach that describes the evolution simultaneously with a competition between the collapse and the azimuthal breakup. Thus, we calculate the collapse time corresponding to the $n = 0$ mode, as well as the breakup times for the other modes characterized by some $n > 0$. The analysis shows that the modes $n = 1$ (off-centre single drop) and $n = 2$ (two drops) are unlikely to be observed, since their breakup time is longer than that of the other modes. The agreement between the LSA results and those obtained using the quasi-static approach shows that the extrapolation of the LSA predictions to advanced stages of the collapse or breakup is appropriate.

Finally, we also report the results of a disjoining pressure model, that includes explicit solid–liquid interaction in the model, but does not allow for contact angle hysteresis. Within this approach a static solution does not exist and we resort to numerical simulations to explore the dynamics. The results obtained using axisymmetric simulations confirm the quasi-static character of the evolution. Furthermore, the nonlinear evolution for non-axisymmetric calculations show good agreement with the growth rates obtained from the LSA for early times; the quality of the agreement extends to later times when comparison with quasi-static model is considered. The final number of drops obtained by the nonlinear simulations under disjoining pressure model is similar to that obtained from the LSA of the slip model for the rings characterized by relatively small aspect ratio. For larger aspect ratios, the disjoining pressure tends to suggest smaller number of drops compared with the

LSA, or ring collapse for some of the configurations where breakup is found under the LSA. As discussed extensively in the paper, this difference is not surprising due to significantly different approaches and techniques employed in these two models.

The work presented here was to a certain degree motivated by experimental results involving breakup of nanoscale liquid metal rings (Wu *et al.* 2010, 2011) and more generally by instabilities leading to self-assembly and directed assembly of liquid metals at the nanoscale (see Herminghaus *et al.* 1998; Favazza, Kalyanaraman & Sureshkumar 2006; Fowlkes *et al.* 2011) which may be of direct relevance to plasmonics and related applications, see Atwater & Polman (2010) for a recent review. We expect that future direct comparison with the experiments will allow us to accurately consider and address some of the questions that are left open in the present work, such as importance of contact angle hysteresis, in addition to more basic questions such as utility of continuum fluid mechanics in providing quantitative description of the nanofluidic phenomena.

We note that in the present work, we do not consider geometries where a breakup in the radial direction might be present, thus leading to concentric rings. This has been observed in experiments with flat liquid metal rings (Wu *et al.* 2011), where the resulting rings individually develop the type of instability described here. Unstable rings have also been observed in the context of films dewetting (Voicu, Harkema & Steiner 2006; Beltrame & Thiele 2010). They result from a radially directed dewetting process that creates consecutively nearly static rings in what one could call radially directed secondary nucleation, similar to the finite length films for planar geometry studied by Diez & Kondic (2007). For instance, in figure 6 of Voicu *et al.* (2006) one can see two rings that break up as in figures 21 and 22; figure 8 of Beltrame & Thiele (2010) shows the case where the inner rings collapse, while the outer ones break up into drops. This sequence of collapses is consistent with our results for ω_{max} shown in figure 16.

Acknowledgements

A.G.G. and J.A.D. acknowledge support from Consejo Nacional de Investigaciones Científicas y Técnicas (CONICET, Argentina) and from Agencia Nacional de Promoción Científica y Tecnológica (ANPCyT, Argentina) with grant PICT 2498/06. L.K. acknowledges partial support by the NSF under grant numbers DMS-1211713 and CBET-1235710.

REFERENCES

- ATWATER, H. A. & POLMAN, A. 2010 Plasmonics for improved photovoltaic devices. *Nat. Mater.* **9**, 205.
- BAROUD, C. N., GALLAIRE, F. & DANGLA, R. 2010 Dynamics of microfluidic droplets. *Lab on a Chip* **10**, 2032.
- BELTRAME, P., KNOBLOCH, E., HANGGI, P. & THIELE, U. 2011 Rayleigh and depinning instabilities of forced liquid ridges on heterogeneous substrates. *Phys. Rev. E* **83**, 016305.
- BELTRAME, P. & THIELE, U. 2010 Time integration and steady-state continuation method for lubrication equations. *SIAM J. Appl. Dyn. Syst.* **9**, 484.
- BONN, D., EGGERS, J., INDEKEU, J., MEUNIER, J. & ROLLEY, E. 2009 Wetting and spreading. *Rev. Mod. Phys.* **81**, 739.
- BOYD, J. P. 2000 *Chebyshev and Fourier Spectral Methods*. Dover.
- CHUGUNOV, S. S., SCHULZ, D. L. & AKHATOV, I. S. 2011 Ring-shaped sessile droplet. In *Proc. ASME 2011 Int. Mech. Eng. Congress*. ASME.

- CONWAY, J., KORNS, H. & FISCH, M. R. 1997 Evaporation kinematics of polystyrene bead suspensions. *Langmuir* **13**, 426.
- CRASTER, R. V. & MATAR, O. K. 2009 Dynamics and stability of thin liquid films. *Rev. Mod. Phys.* **81**, 1131.
- DAVIS, S. H. 1980 Moving contact lines and rivulet instabilities. Part I: the static rivulet. *J. Fluid Mech.* **98**, 225.
- DIEZ, J., GONZÁLEZ, A. G. & KONDIC, L. 2009 On the breakup of fluid rivulets. *Phys. Fluids* **21**, 082105.
- DIEZ, J., GONZÁLEZ, A. G. & KONDIC, L. 2012 Instability of a transverse liquid rivulet on an inclined plane. *Phys. Fluids* **24**, 032104.
- DIEZ, J. & KONDIC, L. 2002 Computing three-dimensional thin film flows including contact lines. *J. Comput. Phys.* **183**, 274.
- DIEZ, J. & KONDIC, L. 2007 On the breakup of fluid films of finite and infinite extent. *Phys. Fluids* **19**, 072107.
- DUSSAN V, E. B. 1976 The moving contact line: the slip boundary condition. *J. Fluid Mech.* **77**, 665.
- FAVAZZA, C., KALYANARAMAN, R. & SURESHKUMAR, R. 2006 Robust nanopatterning by laser-induced dewetting of metal nanofilms. *Nanotechnology* **17**, 4229.
- FOWLKES, J. D., KONDIC, L., DIEZ, J. & RACK, P. D. 2011 Self-assembly versus directed assembly of nanoparticles via pulsed laser induced dewetting of patterned metal films. *Nano Lett.* **11**, 2478.
- DE GENNES, P. G. 1985 Wetting: statics and dynamics. *Rev. Mod. Phys.* **57**, 827.
- GONZÁLEZ, A. G., DIEZ, J., GOMBA, J., GRATTON, R. & KONDIC, L. 2004 Spreading of a thin two-dimensional strip of fluid on a vertical plane: experiments and modeling. *Phys. Rev. E* **70**, 026309.
- GONZÁLEZ, A. G., DIEZ, J., GRATTON, R. & GOMBA, J. 2007 Rupture of a fluid strip under partial wetting conditions. *Europhys. Lett.* **77**, 44001.
- GREENSPAN, H. P. 1978 On the motion of a small viscous droplet that wets a surface. *J. Fluid Mech.* **84**, 125.
- HERMINGHAUS, S., JACOBS, K., MECKE, K., BISCHOF, J., FERY, A., IBN-ELHAJ, M. & SCHLAGOWSKI, S. 1998 Spinodal dewetting in liquid crystal and liquid metal films. *Science* **282**, 916.
- HOCKING, L. M. 1990 Spreading and instability of a viscous fluid sheet. *J. Fluid Mech.* **221**, 373.
- HOCKING, L. M. & MIKSI, M. J. 1993 Stability of a ridge of fluid. *J. Fluid Mech.* **247**, 157.
- KING, J. R., MÜNCH, A. & WAGNER, B. 2006 Linear stability of a ridge. *Nonlinearity* **19**, 2813.
- KOH, Y. Y., LEE, Y. C., GASKELL, P. H., JIMACK, P. K. & THOMPSON, H. M. 2009 Droplet migration: quantitative comparisons with experiment. *Eur. Phys. J. Special Topics* **166**, 117.
- KONDIC, L., DIEZ, J., RACK, P., GUAN, Y. & FOWLKES, J. 2009 Nanoparticle assembly via the dewetting of patterned thin metal lines: understanding the instability mechanism. *Phys. Rev. E* **79**, 026302.
- LANGBEIN, D. 1990 The shape and stability of liquid menisci at solid edges. *J. Fluid Mech.* **213**, 251.
- LIN, T.-S., KONDIC, L. & FILIPPOV, A. 2012 Thin films flowing down inverted substrates: Three-dimensional flow. *Phys. Fluids* **24**, 022104.
- MCGRAW, J. D., LI, J., TRAN, D. L., SHI, A.-C. & DALNOKI-VERESS, K. 2010 Plateau-Rayleigh instability in a torus: formation and breakup of a polymer ring. *Soft Matt.* **6**, 1258.
- MITLIN, V. S. 1993 Dewetting of solid surface: analogy with spinodal decomposition. *J. Colloid Interface Sci.* **156**, 491.
- MÜNCH, A. & WAGNER, B. 2005 Contact-line instability of dewetting thin films. *Physica D* **209**, 178.
- PAIRAM, E. & FERNÁNDEZ-NIEVES, A. 2009 Generation and stability of toroidal droplets in a viscous liquid. *Phys. Rev. Lett.* **102**, 234501.
- PARK, J. & MOON, J. 2006 Control of colloidal particle deposit patterns within picoliter droplets ejected by ink-jet printing. *Langmuir* **22**, 3506.
- PLATEAU, J. 1849 Statique expérimentale et theorique des liquides soumis aux seules forces moléculaires. *Acad. Sci. Bruxelles Mem.* **23**, 5.

- RAYLEIGH, LORD 1879 On the capillary phenomena of jets. *Proc. R. Soc. Lond.* **29**, 71.
- ROY, R. V. & SCHWARTZ, L. W. 1999 On the stability of liquid ridges. *J. Fluid Mech.* **391**, 293.
- SAVVA, N. & KALLIADASIS, S. 2011 Dynamics of moving contact lines: a comparison between slip and precursor film models. *Europhys. Lett.* **94**, 64004.
- SCHAFLE, C., BRINKMANN, M., BECHINGER, C., LEIDERER, P. & LIPOWSKY, R. 2010 Morphological wetting transitions at ring-shaped surface domains. *Langmuir* **26**, 11878.
- SEKIMOTO, K., OGUMA, R. & KAWASAKI, K. 1987 Morphological stability analysis of partial wetting. *Ann. Phys. (N.Y.)* **176**, 359.
- SQUIRES, T. M. & QUAKE, S. R. 2005 Microfluidics: fluid physics at the nanoliter scale. *Rev. Mod. Phys.* **77**, 977.
- STONE, H. A., STROOCK, A. D. & AJDARI, A. 2004 Engineering flows in small devices. *Annu. Rev. Fluid Mech.* **36**, 381.
- THIELE, U. 2010 Thin film evolution equations from (evaporating) dewetting liquid layers to epitaxial growth. *J. Phys. Condens. Matter* **22**, 084019.
- THIELE, U. & KNOBLOCH, E. 2003 Front and back instability of a liquid film on a slightly inclined plate. *Phys. Fluids* **15**, 892.
- VOICU, N. E., HARKEMA, S. & STEINER, U. 2006 Electric-field-induced pattern morphologies in thin liquid films. *Adv. Funct. Mater.* **16**, 926.
- WORTHINGTON, A. M. 1879 On the spontaneous segmentation of a liquid annulus. *Proc. R. Soc. Lond.* **30**, 49.
- WU, Y., FOWLKES, J. D., RACK, P. D., DIEZ, J. A. & KONDIC, L. 2010 On the breakup of patterned nanoscale copper rings into droplets via pulsed-laser-induced dewetting: competing liquid-phase instability and transport mechanisms. *Langmuir* **26**, 11972.
- WU, Y., FOWLKES, J. D., ROBERTS, N. A., DIEZ, J. A., KONDIC, L., GONZÁLEZ, A. G. & RACK, P. D. 2011 Competing liquid phase instabilities during pulsed laser induced self-assembly of copper rings into ordered nanoparticle arrays on SiO₂. *Langmuir* **27**, 13314.
- YANG, L. & HOMSY, G. M. 2006 Steady three-dimensional thermocapillary flows and dryout inside a V-shaped wedge. *Phys. Fluids* **18**, 042017.